

# Satellite galaxies in hydrodynamical simulations of Milky Way sized galaxies

Markus Wadepuhl<sup>\*1</sup> and Volker Springel<sup>1,2,3</sup>

<sup>1</sup>Max-Planck-Institut for Astrophysics, Karl-Schwarzschild-Strasse 1, 85740 Garching bei München, Germany

<sup>2</sup>Heidelberg Institute for Theoretical Studies, Schloss-Wolfsbrunnengasse 35, 69118 Heidelberg, Germany

<sup>3</sup>Zentrum für Astronomie der Universität Heidelberg, Mönchhofstr. 12-14, 69120 Heidelberg, Germany

28 April 2010

## ABSTRACT

Collisionless simulations of the CDM cosmology predict a plethora of dark matter substructures in the halos of Milky Way sized galaxies, yet the number of known luminous satellite galaxies is very much smaller, a discrepancy that has become known as the ‘missing satellite problem’. The most massive substructures have been shown to be plausibly the hosts of the brightest satellites, but it remains unclear which processes prevent star formation in the many other, purely dark substructures. We use high-resolution hydrodynamic simulations of the formation of Milky Way sized galaxies in order to test how well such self-consistent models of structure formation match the observed properties of the Galaxy’s satellite population. For the first time, we include in such calculations feedback from cosmic rays injected into the star forming gas by supernovae as well as the energy input from supermassive black holes growing at the Milky Way’s centre and its progenitor systems. We find that non-thermal particle populations quite strongly suppress the star formation efficiency of the smallest galaxies. In fact, our cosmic ray model is able to reproduce the observed faint-end of the satellite luminosity function, while models that include only the effects of cosmic reionization, or galactic winds, do significantly worse. Our simulated satellite population approximately matches available kinematic data on the satellites and their observed spatial distribution. We conclude that a proper resolution of the missing satellite problem likely requires the inclusion of non-standard physics for regulating star formation in the smallest halos, and that cosmic reionization alone may not be sufficient.

**Key words:** methods: numerical – galaxies – cosmology: dark matter

## 1 INTRODUCTION

The leading  $\Lambda$ CDM cosmology predicts that galaxies form hierarchically in a ‘bottom up’ fashion (e.g. White & Rees 1978; Longair 1999), where small perturbations in the dark matter density distribution collapse earlier than larger perturbations, and low-mass halos grow by smooth accretion or mergers with other halos, successively building up ever bigger structures. But structures falling into bigger systems during this process are not always disrupted completely. As N-body simulations show, the inner cores of infalling objects often survive the various disruptive effects acting on them, like tidal truncation, tidal shocking or ram-pressure stripping. It is believed that the observed dwarf galaxies orbiting around the Milky Way (MW) are examples of such surviving remnants.

Based on the first generation of very high resolu-

tion collisionless CDM simulations, Klypin et al. (1999) and Moore et al. (1999) pointed out a very striking apparent discrepancy between theoretical predictions for such satellite systems and actual observations. Given the very large number of predicted dark matter substructures, there appears to be a dearth of luminous satellites in the Milky Way. In fact, the cumulative number of observed satellite galaxies and of predicted substructures above a given circular velocity value differed by a factor of  $\sim 10$ . This has become known as the ‘missing satellite problem’.

The initial analysis of Moore et al. (1999) and Klypin et al. (1999) may have overstated the magnitude of the discrepancy, both because of uncertainties in assigning correct circular velocity values to the observed satellites (Stoehr et al. 2002) and because a number of additional faint satellites have been discovered meanwhile in the MW (see for example Irwin et al. 2007; Liu et al. 2008; Martin et al. 2008; Simon & Geha 2007; Grebel 2000; van den Bergh 2000; Belokurov et al. 2008,

\* E-mail: wadepuhl@mpa-garching.mpg.de

2009; Watkins et al. 2009; Belokurov et al. 2010). However, there is a consensus that the many low-mass satellites predicted by the N-body simulations need to be strongly suppressed in luminosity, otherwise a significant discrepancy with the observed satellite luminosity functions results, that, if confirmed, may in principle even be used to rule out cold dark matter.

With increasing numerical resolution, the missing satellite problem has become more acute. Modern cosmological dark matter simulations of Milky Way sized halos (Diemand et al. 2008; Springel et al. 2008; Stadel et al. 2009) resolve up to  $\sim 300,000$  dark matter substructures, while the number of observed satellite galaxies still comprises just a few dozens. We note that the modern dark matter only simulations are even able to resolve substructures inside substructures, and interestingly, there is also some observational evidence for a satellite possibly orbiting around another satellite (Belokurov et al. 2008).

Klypin et al. (1999) did not only raise the missing satellite problem, they were also among the first to suggest a potential solution to this issue. In particular, they proposed that star formation inside low mass halos could be suppressed because of photo evaporation of gas due to a strong intergalactic ionizing UV background. This would keep most of the orbiting satellites dark and render them visually unobservable. Indeed, the simple filtering mass model of Gnedin (2000) for the impact of a UV background on the cooling efficiency of small halos predicts a quite sizable effect, with a nearly complete suppression of cooling in all halos with circular velocity below  $50 \text{ km s}^{-1}$ . However, recent full hydrodynamical simulations have not confirmed this (Hoeft et al. 2006; Okamoto et al. 2008). They find a considerably weaker effect, where only halos with circular velocities less than  $\sim 25 \text{ km s}^{-1}$  are affected. This also casts some doubt about the faint-end results of numerous semi-analytic models for the satellite population (e.g. Benson et al. 2002; Kravtsov et al. 2004), which typically employed the filtering mass formalism and hence assumed an overly strong effect of the UV background. We will reexamine this question in this work based on our cosmological hydrodynamic simulations of Milky Way formation, which include a treatment of cosmic reionization.

Another possible solution for the satellite problem was proposed by Strigari et al. (2007) who suggested that not the satellite mass at the present epoch determines whether a satellite would be luminous or not, but rather the maximum mass it had before accretion onto the Milky Way's halo. This is based on the idea that tidal stripping and ram pressure unbinds the gas from an infalling satellite and thus stalls any further star formation. With this assumption, the stellar mass at the time of accretion is essentially retained until the present epoch, and it becomes a question of allowing high-redshift star formation only in satellites above a sufficiently high mass threshold.

A more radical conjecture is that the properties of the dark matter particles may have to be changed. Instead of having negligible velocity dispersion at the time of decoupling, we may instead be dealing with (slightly) warm dark matter (WDM). This can suppress the abundance of low mass structure considerably (e.g. Colin et al. 2000), but provided the particle mass is not lower than  $\sim 1 \text{ keV}$  a sufficiently large number of substructures still survives to ex-

plain the observed satellite abundance (Macciò & Fontanot 2010).

In the most recent works on the subject, a number of interesting and encouraging results have been obtained. Observationally, it has been discovered that the satellites all have approximately the same central mass density (within 300 to 600 pc), independent of their luminosity (Gilmore et al. 2007; Strigari et al. 2008). Explaining this central density threshold has become an important additional challenge for theoretical models. Also, a significant number of new faint satellites have been discovered with the help of the SDSS (Irwin et al. 2007; Liu et al. 2008; Martin et al. 2008; Simon & Geha 2007; Grebel 2000; van den Bergh 2000; Belokurov et al. 2008, 2009; Watkins et al. 2009; Belokurov et al. 2010), improving our knowledge about the full satellite population significantly, but at the same time also raising the question whether we may perhaps still be missing large numbers of satellites at ultra low surface brightnesses.

On the theoretical side, refined treatments of the effects of reionization, often coupled to the results of high-resolution collisionless simulations have been used to model the satellite population. Macciò et al. (2010) employed a number of different semi-analytic models and low-resolution hydrodynamic simulations to study the satellite luminosity function. Despite just invoking photoheating as primary feedback process, they achieved reasonable agreement for some of their models, leading them to argue that the satellite problem may be solved. Similarly, Li et al. (2010) invoked a strong impact of reionization in a semi-analytic model similar to those applied to the Millennium Simulation (Croton et al. 2006) to reproduce the luminosity function of galaxies around the Milky Way. Busha et al. (2010) used simple prescriptions for the impact of inhomogeneous reionization on the satellite population, pointing out that subtle changes in the assumptions about how reionization affects star formation in small galaxies can lead to large changes in the predicted number of satellites.

Recently, Strigari et al. (2010) examined the kinematics of five well-measured Milky Way satellite galaxies and compared them to dark matter satellites of the high-resolution simulations of the Aquarius Project (Springel et al. 2008). They showed that these systems are fully consistent with  $\Lambda$ CDM expectations and may be hosted in cored dark matter structures with maximum circular velocities in the range  $10$  to  $30 \text{ km s}^{-1}$ . Interestingly, Bullock et al. (2009) pointed out that the number of real satellite systems may in fact be much larger than commonly believed, with the majority of them being so far undetected because of their low surface brightness. In this scenario, the ‘common mass scale’ inferred for the observed satellites may in fact just arise from a selection bias.

The first high-resolution hydrodynamic simulation able to directly resolve the satellite population has recently been presented by Okamoto & Frenk (2009). They argue that the common mass scale identified in the observations arises from early reionization at redshift around  $z \sim 12$ , and that satellites that have not yet grown to a maximum circular velocity of  $\sim 12 \text{ km s}^{-1}$  *by the time of reionization*, will not be able to make any stars later on. Even if they grow above this threshold, Okamoto & Frenk (2009) predict them to remain dark.

Despite all of this progress, it is evident that there remain many open questions concerning the population of faint and ultra-faint satellite galaxies orbiting around Milky Way like galaxies. Especially the influence of different baryonic feedback processes on the luminosity function of the simulated satellites has not been investigated in sufficient detail. It is therefore far from clear whether photoheating from a UV background and ordinary supernovae feedback are indeed the correct physical solutions to the missing satellite problem. In fact, the in part contradictory results that have been obtained with analytic recipes to describe the impact of reionization suggest that more accurate methodologies are required to reliably settle the issue.

We have therefore embarked on a research program where we use high-resolution hydrodynamic simulations of the formation of Milky Way-sized halos to shed more light on these questions, in particular by investigating a variety of feedback processes known to be important in galaxy formation. Besides the impact of reionization, these include galactic winds and outflows, energy input by growing supermassive black holes, or the non-thermal support of gas by cosmic rays or magnetic fields. Ultimately we aim to reach similar numerical resolution as has been obtained for recent collisionless simulations, even though this goal may still be several years away.

In this work, we present some of our first results. We use several well resolved hydrodynamical simulations of the formation of a Milky Way sized galaxy to investigate the properties of the predicted population of satellite galaxies, for different choices of the included physics. Besides a default reference model that includes only a treatment of radiative cooling, star formation, and cosmic reionization, we consider also models that add galactic winds, supermassive black hole growth, or cosmic ray injection by supernovae shock waves. By comparing the simulation results with a comprehensive catalogue of the known Milky Way satellites, we seek to determine which of these processes is most important in shaping the satellite population.

This paper is organized as follows. In Section 2, we describe the methodological details of our simulations, while the observational knowledge about the satellites is briefly summarized in Section 3. Sections 4, 5 and 6 present the results for our simulated populations of satellite galaxies, both with respect to individual satellite histories as well as with respect to their population as a whole. Our conclusions are summarized in Section 7.

## 2 METHODOLOGY

Our simulations are based on initial conditions originally constructed for the Aquarius Project (Springel et al. 2008) of the Virgo Consortium. This project carried out highly resolved dark matter only simulations of 6 different Milky Way-sized halos, at a variety of different numerical resolutions. In the nomenclature of Springel et al. (2008), the halo and resolution level investigated here is called ‘Aq-C-4’, and has about 5.4 million dark matter particles in the final virial radius. The same object has also been studied in the hydrodynamic simulations of Scannapieco et al. (2009), albeit at the considerably lower resolution (by a factor 8 in particle number) corresponding to ‘Aq-C-5’. There it was found that

this ‘C’-halo produced the lowest bulge-to-disk ratio among the 6 candidate halos selected in the Aquarius Project, making it a particularly good candidate for the formation of a large disk galaxy. We note, however, that we do not expect our choice of target halo to influence our principal conclusions for the satellite population.

In this paper, we model the gas component with smoothed particle hydrodynamics (SPH) and introduce the gas particles into the initial conditions by splitting each original particle into a dark matter and gas particle pair, displaced slightly with respect to each other (at fixed center-of-mass) to arrive at a regular distribution of the mean particle separations, and with a mass ratio corresponding to a baryon fraction of 16 per cent. The cosmological parameters are  $\Omega_m = 0.25$ ,  $\Omega_\Lambda = 0.75$ ,  $\sigma_8 = 0.9$  and  $h = 0.73$ , the same ones used as in the original Aquarius simulations, which are consistent with the WMAP1 cosmological constraints. A periodic box of size  $100 h^{-1} \text{Mpc}$  on a side is simulated, with varying spatial resolution that ‘zooms in’ on the formation of a single galaxy. In the high-resolution region, we reach a mass simulation of  $\approx 2 \times 10^5 h^{-1} M_\odot$  and  $\approx 2 \times 10^4 h^{-1} M_\odot$  for dark matter and gas particles, respectively. A constant comoving gravitational softening length of  $\epsilon = 0.25 h^{-1} \text{kpc}$  was used for all high-resolution particles.

We employed the parallel TreeSPH code GADGET-3 for our runs, which is an improved and extended version of GADGET-2 (Springel 2005). GADGET calculates the long-range gravitational field in Fourier space, and the short range forces in real space with a hierarchical multipole expansion, based on a tree. This approach guarantees a homogeneously high spatial resolution in the gravitational force calculation and can be efficiently combined with an individual timestep integration scheme. For the hydrodynamics, GADGET uses the ‘entropy formulation’ of SPH (Springel & Hernquist 2002), which is derived from a variational principle and simultaneously conserves energy and entropy where appropriate.

In the hydrodynamic part of GADGET, different physical processes besides ordinary gas dynamics are calculated. Most importantly, these are radiative cooling, star formation and its regulation by supernovae feedback processes (Springel & Hernquist 2003). The code can optionally also model black hole growth and (Springel et al. 2005) and cosmic ray physics (Jubelgas et al. 2008). We shall now briefly describe the physics modules we used.

### 2.1 Star formation model

Radiative cooling is followed for a primordial mixture of helium and hydrogen under the assumption of collisional ionization equilibrium, using a formulation as in Katz et al. (1996). A spatially uniform, ionizing UV background is introduced with an amplitude and time evolution described by an updated version of Haardt & Madau (1996), leading to reionization of the universe by redshift  $z \simeq 6$ .

To model star formation, we use the hybrid multiphase model for star formation and supernova feedback introduced by Springel & Hernquist (2003), in which every sufficiently dense gas particle is treated as a representative region for the multiphase structure of the interstellar medium (ISM). These hybrid particles are pictured to be comprised of cold dense clouds in pressure equilibrium with a hot ambient gas

phase, where only the clouds contribute material available for star formation. Mass and energy exchange processes between these two phases are computed by simple differential equations, as described in Springel & Hernquist (2003), giving rise to an effective equation of state that regulates the dense gas of the ISM. Collisionless star particles are spawned stochastically from this star-forming phase according to a local estimate of the star formation rate. The gas consumption timescale of the model is calibrated such that it reproduces the Kennicutt law (Kennicutt 1989) between star formation rate and gas surface density observed in low-redshift disk galaxies.

## 2.2 Wind model

Even though the above ISM model reproduces the star formation rates observed in disk galaxies, it overproduces the total amount of stars formed when applied in cosmological simulations. This is likely related to its inability to reproduce the observed galaxy-scale outflows seen around many starbursting galaxies. We have therefore also investigated the phenomenological model for galactic winds introduced by Springel & Hernquist (2003). We adopted a constant wind velocity of  $v_{\text{wind}} = 484 \text{ km s}^{-1}$  and mass loading factor of  $\eta = 2$ , i.e. the mass flux of the wind is twice the star formation rate. Individual gas particles were stochastically added to the galactic wind by changing their velocity to the prescribed wind velocity. We adopted an anisotropic distribution for the wind direction, launching it preferentially perpendicular to the disk.

The wind model causes an outflow of gas from the dense gaseous disc, transporting energy, matter and heavy elements out of the disc in proportion to the star formation rate. Not only the central galaxy is affected by the winds, all the star forming satellite galaxies produce winds, which will more quickly deplete their gas content. The effect of galactic winds is actually expected to be more effective in these low mass systems as their potential well is much shallower than the one of the main galaxy (Dekel & Silk 1986), which should increase the mass loss due to outflows. Including winds in the simulation thus appears in principle promising as a mechanism to reduce the number of luminous satellites, but the effect may sensitively depend on how the wind properties are scaled with galaxy size (e.g. Oppenheimer & Davé 2006).

## 2.3 Black hole model

Supermassive black holes are thought to reside at the centres of most if not all spheroidal galaxies. The tight relation between their masses and the velocity dispersion of their hosting galaxies suggest a tight evolutionary link, which is probably established by a self-limited growth mechanism in which the energy output of a growing black hole eventually terminates its further growth and the surrounding star formation, for example by expelling gas from the central region of the galaxy. Hydrodynamical simulation models have been successfully used to model this process in detail (Di Matteo et al. 2005; Springel et al. 2005), and led to quite successful unified models of the formation of spheroidal galaxies (Hopkins et al. 2006).

While it is unclear whether the influence of the Milky Way's black hole has affected the formation of other components of the Galaxy besides the central bulge, it appears possible that the heating effects from different quasar episodes during the growth history of the MW's supermassive black hole have had an impact on the satellite population as well, for example by heating the environment of progenitor halos through strong quasar driven outflows. Indeed, in theoretical models outflow feedback has been found to be violent enough to be able to strongly affect even neighbouring galaxies (Scannapieco et al. 2001; Thacker et al. 2002).

To study such effects, we have adopted the techniques introduced by Springel et al. (2005) for tracking black hole growth and its associated energy feedback in cosmological simulations. In brief, we periodically call a FoF group finding algorithm that identifies newly formed halos that do not contain a black hole yet. If such a halo is sufficiently massive, its densest gas particle is converted to a black hole seed of mass  $M_{\text{BH}} = 10^5 h^{-1} M_{\odot}$ . The black hole particles are treated as sinks particles that accrete gas from their surroundings at a rate estimate with a simple Bondi-Hoyle prescription, limited to the Eddington rate. The black hole accretion is assumed to have a fixed radiative efficiency of  $0.1 \dot{M} c^2$ , and 5% of the produced radiation are assumed to couple thermally to the gas surrounding the black hole. This energy feedback can eventually drive a quasar-driven outflow and regulates the mass growth of the black holes. We also allow for two black holes to merge with each other once they get sufficiently close to each other.

## 2.4 Cosmic ray model

In the interstellar medium of our own Galaxy, it is believed that thermal pressure, cosmic rays and magnetic fields are roughly in equipartition. Even though it is hence known that non-thermal particle populations play an important role in regulating the gas dynamics of the ISM, this component has usually been ignored in studies of galaxy formation. The cosmic ray particles may originate in acceleration processes in high Mach number shocks in supernova remnants or could be produced in structure formation shock waves. We here focus on cosmic ray injection associated with supernovae, and consider only Coulomb and hadronic interactions as loss processes for the cosmic ray particles (Enßlin et al. 2007).

A numerical treatment of the cosmic ray component is rather complicated as in principle their full, in general anisotropic distribution function has to be modeled. Also, the motion of the cosmic ray fluid is tightly coupled to the magnetic field, which in turn is non-trivial to calculate accurately. We therefore employ the subresolution model described by Jubelgas et al. (2008), which has already been successfully employed in previous work (Pfrommer et al. 2007, 2008; Pfrommer 2008).

The basic assumption of our CR model (Enßlin et al. 2007; Jubelgas et al. 2008) is that the momentum spectrum of cosmic rays can be well represented by a simple power law of the form

$$\frac{d^2 N}{dp dV} = C p^{-\alpha} \theta(p - q), \quad (1)$$

where  $C$  gives the normalization,  $q$  is a low momentum cutoff, and  $\alpha$  is the power law slope. We assume that the cosmic

Label	Mass resolution (gas)	Gravitational softening	Physics
Ref	$5.14 \times 10^4 M_{\odot}$	0.34 kpc	star formation, supernova feedback <sup>(a)</sup>
BH	$5.14 \times 10^4 M_{\odot}$	0.34 kpc	star formation, supernova feedback <sup>(a)</sup> , AGN feedback <sup>(b)</sup>
Wind	$5.14 \times 10^4 M_{\odot}$	0.34 kpc	star formation, supernova feedback <sup>(a)</sup> , galactic winds <sup>(a)</sup>
CR	$5.14 \times 10^4 M_{\odot}$	0.34 kpc	star formation, supernova feedback <sup>(a)</sup> , AGN feedback <sup>(b)</sup> , cosmic rays <sup>(c)</sup>
LowRes	$4.11 \times 10^5 M_{\odot}$	0.68 kpc	star formation, supernova feedback <sup>(a)</sup> , AGN feedback <sup>(b)</sup>

**Table 1.** Overview of the simulations used in this work. The label of each simulation will be used throughout the rest of this paper. The different physics models we use are described in detail in (a) Springel & Hernquist (2003), (b) Springel et al. (2005), and (c) Jubelgas et al. (2008).

rays are dominated by protons, and that the local magnetic field is sufficiently tangled to effectively lock in the CRs to the gas. The pressure of the cosmic ray population is then given by

$$P_{\text{CR}} = \frac{C m_p C^2}{6} \mathcal{B}_{\frac{1}{1+q^2}} \left( \frac{\alpha-2}{2}, \frac{3-\alpha}{2} \right), \quad (2)$$

while the number density is simply  $n_{\text{CR}} = C q^{1-\alpha}/(\alpha-1)$ . Here

$$\mathcal{B}_n(a, b) \equiv \int_0^n x^{a-1} (1-x)^{b-1} dx \quad (3)$$

denotes incomplete Beta functions. Based on the findings of Jubelgas et al. (2008), we expect this additional pressure to be especially influential in low mass satellites, because it here can substantially reduce the density of the ISM. This should effectively reduce the number of low luminosity satellites.

We model the decay of the cosmic ray population by accounting for coulomb cooling and catastrophic hadronic losses as described in Jubelgas et al. (2008). Note that the ‘cosmic ray cooling’ mediated by these effects can occur on a different timescale as the ordinary thermal cooling. In particular, gas can end up being cosmic ray pressure supported after having lost much of its thermal support through radiative cooling. Finally, we adopt a simple source function for the injection of new cosmic ray particles, which we link directly to the star formation rate. This is motivated by observations of supernova remnants (Aharonian et al. 2006), where a large fraction of the supernovae energy is seen to initially appear as cosmic rays.

## 2.5 Simulation set and analysis

In Table 1, we summarize the primary properties of the simulations we analyze in this work. We consider four different high-resolution simulations of the same initial conditions, corresponding to the Aq-C-4 halo, but carried out with different physics in the baryonic sector. Our reference calculation (labeled ‘REF’) includes star formation and supernova feedback as described by our multi-phase model, as well as ordinary radiative cooling and heating by a UV background that reionizes the universe by redshift  $z = 6$ . We have repeated this calculation by adding in turn each of the three additional feedback models described above. This yields the three simulations ‘BH’ (with black hole growth and feedback), ‘WIND’ (with the phenomenological wind model), and ‘CR’ (with cosmic ray physics). Our primary simulation set is composed of these four simulations. They are of equal numerical resolution and hence allow a relatively clean assessment of the impact of the different physics components

on the satellite population. We note that our primary aim in this work is not to construct a best-fitting model for the Milky Way, as this may require a combination of the different physics models and a fine-tuning of their free parameters. Rather we want to highlight the importance of different physics for the satellite population.

We also briefly consider a further simulation, labeled ‘LOWRES’. This is a rerun of our reference model at lower resolution, corresponding to ‘Aq-A-5’. We use this simulation for an assessment of the numerical resolution and convergence limits of our simulations.

To analyze the time evolution of the simulated galaxies, several snapshots were stored at different times. As a basic analysis step, the snapshots were first processed by a group finding algorithm in order to identify individual halos. The group finding was done with a simple friend-of-friends (FOF) algorithm applied only to the dark matter particles with a linking length equal to 20% of their mean particle spacing. The gas and star particles were linked to their nearest dark matter particle. Next, each halo found in the first step was subjected to a substructure detection procedure, for which we used the SUBFIND algorithm (Springel et al. 2001) in a version extended to allow a treatment of gas as well (Dolag et al. 2009). SUBFIND calculates the local density everywhere and searches for substructure candidates that are locally overdense. It then computes the gravitational potential at the positions of all particles in the candidate structures, and determines the subset of particles that are gravitationally bound. In this way, only real physical structures are found. To avoid noise from substructures composed of only a few particles, only substructures containing at least 20 particles were kept for further analysis.

The gravitationally bound structures found by SUBFIND in this way form our catalogue of simulated galaxies, including both central galaxies as well as genuine satellites. For the simulated galaxies, we applied a stellar population synthesis model (Bruzual & Charlot 2003) to estimate their luminosities and colours, based on the formation times and masses of the star particles created in the simulations. We made no attempt to account for the metallicity dependence of the stellar population synthesis model or dust corrections.

## 3 OBSERVATIONAL KNOWLEDGE

Before we present our simulation results, we summarize in this section the most recent observational data with respect to the Milky Way’s satellite population. We will later use this comprehensive catalogue of the known satellites to-

Label	$\alpha_{2000}$	$\delta_{2000}$	D (kpc)	$M_{V,tot}$ (mag)	$\mu_{0,V}$ (mag/arcsec <sup>2</sup> )	Mass ( $10^6 M_{\odot}$ )
BooI <sup>(e)</sup>	14 <sup>h</sup> 00 <sup>m</sup>	+14°30′	66 ± 3	−6.3 ± 0.2	27.5 ± 0.3	–
BooII <sup>(e)</sup>	13 58	+12 51	42 ± 8	−2.7 ± 0.9	28.1 ± 1.6	–
Carina <sup>(b)</sup>	60 42	−50 58	101 ± 5	−9.3	25.5 ± 0.4 <sup>(h)</sup>	13
Com <sup>(e)</sup>	12 27	+23 54	44 ± 4	−4.1 ± 0.5	27.3 <sup>+0.7</sup> <sub>−0.6</sub>	1.2 ± 0.4 <sup>(f)</sup>
CVnI <sup>(e)</sup>	13 28	+33 33	218 ± 10	−8.6 <sup>+0.2</sup> <sub>−0.1</sub>	27.1 ± 0.2	27 ± 4 <sup>(f)</sup>
CVnII <sup>(e)</sup>	12 57	+34 19	160 <sup>+4</sup> <sub>−5</sub>	−4.9 ± 0.5	26.1 <sup>+0.7</sup> <sub>−0.6</sub>	2.4 ± 1.1 <sup>(f)</sup>
Draco <sup>(e)</sup>	17 20	+57 55	76 ± 5	−8.8 ± 0.2	25.5 ± 0.2	22
Fornax <sup>(b)</sup>	02 40	−34 27	138 ± 8	−13.2	23 ± 0.3 <sup>(h)</sup>	68
Her <sup>(e)</sup>	16 31	+12 48	132 ± 12	−6.6 ± 0.3	27.2 <sup>+0.6</sup> <sub>−0.5</sub>	7.1 ± 2.6 <sup>(f)</sup>
LeoA <sup>(b)</sup>	09 59	+30 45	690 ± 100	−11.4	–	11
LeoI <sup>(b)</sup>	10 08	+12 19	250 ± 30	−11.9	22.4 ± 0.3 <sup>(h)</sup>	22
LeoII <sup>(b)</sup>	11 13	+22 09	205 ± 12	−9.6	24.0 ± 0.3 <sup>(h)</sup>	9.7
LeoIV <sup>(e)</sup>	11 33	−00 32	160 <sup>+15</sup> <sub>−14</sub>	−5.0 <sup>+0.6</sup> <sub>−0.5</sub>	27.5 <sup>+1.3</sup> <sub>−1.2</sub>	1.4 ± 1.5 <sup>(f)</sup>
LeoV <sup>(j)</sup>	11 31	+02 13	180	−4.3	27.5 ± 0.5	–
LeoT <sup>(e)</sup>	09 35	+17 03	407 ± 38	−7.1 <sup>(c)</sup>	26.9 <sup>(c)</sup>	8.2 ± 3.6 <sup>(f)</sup>
LiuI <sup>(d)</sup>	10 00	+57 30	83.2 <sup>+9.3</sup> <sub>−8.4</sub>	−4.15	28.8	–
LiuII <sup>(d)</sup>	13 29	+28 41	75.9 <sup>+8.5</sup> <sub>−7.6</sub>	−3.91	29.2	–
LMC <sup>(a)</sup>	05 24	−69 50	49	−18.5 <sup>(i)</sup>	20.7 ± 0.1 <sup>(h)</sup>	10.000 <sup>(g)</sup>
NGC6822 <sup>(b)</sup>	19 45	−14 48	490 ± 40	−15.2	21.4 ± 0.2 <sup>(h)</sup>	1640
Pegasus <sup>(b)</sup>	23 29	+14 45	955 ± 50	−12.9	–	58
Phoenix <sup>(b)</sup>	01 51	−44 27	445 ± 30	−10.1	–	33
PscI <sup>(l)</sup>	23 19	0 0	80	–	–	0.1
PscII <sup>(m)</sup>	22 58	5 57	180	−5.0	–	–
Sag <sup>(b)</sup>	18 55	−30 29	24 ± 2	−13.4	25.4 ± 0.2 <sup>(h)</sup>	150 <sup>(i)</sup>
Sculpor <sup>(b)</sup>	01 00	−72 50	79 ± 4	−11.1	23.7 ± 0.4 <sup>(h)</sup>	6.4
Seg1 <sup>(e)</sup>	10 07	+16 04	23 ± 2	−1.5 <sup>+0.6</sup> <sub>−0.8</sub>	27.6 <sup>+1.0</sup> <sub>−0.7</sub>	–
Seg2 <sup>(k)</sup>	02 19	+20 10	35	−2.5 ± 0.2	–	0.55 <sup>+1.1</sup> <sub>−0.3</sub>
Seg3 <sup>(m)</sup>	21 21	+19 07	16	−1.2	–	–
Sextans <sup>(b)</sup>	10 13	−01 37	86 ± 4	−9.5	26.2 ± 0.5 <sup>(h)</sup>	19
SMC <sup>(a)</sup>	00 51	−73 10	58	−17.1 <sup>(i)</sup>	22.1 ± 0.1 <sup>(h)</sup>	400 <sup>(g)</sup>
Tucana <sup>(b)</sup>	22 42	−64 25	880 ± 40	−9.6	25.1 ± 0.1 <sup>(h)</sup>	–
UMaI <sup>(e)</sup>	10 35	+51 55	96.8 ± 4	−5.5 ± 0.3	27.7 <sup>+0.5</sup> <sub>−0.4</sub>	15 ± 4 <sup>(f)</sup>
UMaII <sup>(e)</sup>	08 07	+63 07	30 ± 5	−4.2 ± 0.5	27.9 ± 0.6	4.9 ± 2.2 <sup>(f)</sup>
UMi <sup>(b)</sup>	15 09	+67 13	66 ± 3	−8.9	25.5 ± 0.5 <sup>(h)</sup>	23
Will <sup>(e)</sup>	10 49	+51 03	38 ± 7	−2.7 ± 0.7	26.1 ± 0.9	–

**Table 2.** Compilation of all presently known Milky Way satellite galaxies. The values are taken from the following studies: (a) van den Bergh (1994), (b) Mateo (1998), (c) Irwin et al. (2007), (d) Liu et al. (2008), (e) Martin et al. (2008), (f) Simon & Geha (2007), (g) Bekki (2008), (h) Grebel (2000), (i) van den Bergh (2000), (j) Belokurov et al. (2008), (k) Belokurov et al. (2009), (l) Watkins et al. (2009), (m) Belokurov et al. (2010). All errors are from the corresponding papers. The different columns list the position in galactic coordinates, the proper distance, the total V-band magnitude, the surface brightness and the total estimated mass of the individual satellites.

gether with predictions for their total number over the whole sky when comparing with our simulations.

Table 2 gives a compilation of the properties of all Milky Way satellites known today. The basic data of the ‘classical’ satellites, which were already known in 1998, are given by Mateo (1998) and were only slightly extended using van den Bergh (2000) who updated the data on the Small and the Large Magellanic Cloud (SMC and LMC, respectively). Up to this time, the number of known satellites was just 16, but during the differ-

ent data releases<sup>\*</sup> (York et al. 2000; Willman et al. 2002) of the Sloan Digital Sky Survey (SDSS), the number of known satellites increased significantly thanks to new discoveries made with the survey. Table 2 includes the new satellite galaxies found with SDSS (Willman et al. 2005a,b; Zucker et al. 2006b; Belokurov et al. 2006; Zucker et al. 2006a; Belokurov et al. 2007; Irwin et al. 2007; Walsh et al. 2007; Liu et al. 2008; Walsh et al. 2008; Belokurov et al. 2008, 2009; Watkins et al. 2009; Belokurov et al. 2010), us-

<sup>\*</sup> <http://www.sdss.org/dr6/index.html>

ing the recently published structural parameters given in Martin et al. (2008). To estimate the half light radius of the Large Magellanic Cloud, the formula  $r_h = 1.68 r_e$  (Martin et al. 2008) was adopted.

Up to now, there are 35 known Milky Way satellites. However, this sample is not complete, as the recently found satellites are all limited to the area of the sky covered by SDSS, which corresponds to a fraction of 0.194 of the full sky. Effectively, only this region of the whole sky has been scanned for faint satellites (see Tollerud et al. 2008). Taking into account the detection limits and the sky coverage of the SDSS survey, Simon & Geha (2007) estimate the number of satellite galaxies with a surface brightness above  $\approx 28$  mag/arcsec<sup>2</sup> (Martin et al. 2008) expected over the whole sky to be 57. However, more recent works favor a limit of 30 mag/arcsec<sup>2</sup> (Bullock et al. 2009), which we adopt throughout the rest of this paper. Using this threshold, we denote simulated satellite galaxies as ‘observable’ if their surface brightness exceeds 30 mag/arcsec<sup>2</sup>.

#### 4 ABUNDANCE OF LUMINOUS SATELLITES

Arguably the most fundamental property of the subhalo population is the abundance of satellites as a function of luminosity. In Figure 1, we show the differential luminosity function of the simulated satellite galaxies for our four primary simulations, and compare to the observations for the Milky Way. The latter are expressed in terms of the fitting formula given by Koposov et al. (2008):

$$\frac{dN}{dM_V} = 10 \times 10^{0.1(M_V+5)}. \quad (4)$$

The upper left panel of Figure 1 shows our result for the reference simulation. There is a sizable offset between the simulated and the observed luminosity functions, shown in black and green, respectively. Satellites with large stellar masses are even more strongly overproduced than low luminosity ones. This shows that photoheating and supernova feedback as included in the reference model are insufficient to match the observed satellite abundance.

The other panels of the figure show the results we obtained for our alternative physics simulations. As one might expect, including supermassive black holes has no substantial influence on the population of satellites, yielding essentially the same result as for our reference simulation. This shows that environmental heating effects from quasar feedback, in particular the possible quenching of star formation in nearby small halos, play no important role in the history of the Aq-C halo. Interestingly, galactic outflows with our standard wind prescription are also unable to significantly improve the agreement with the observations. While the most luminous satellites are moderately suppressed in stellar mass, the satellites tend to pile up on the faint side of the luminosity function, yielding to a slight steepening effect of the luminosity function, quite different from what is needed to match the data. Finally, the simulation including cosmic rays yields a substantial modification of the results. Here we actually obtain very good agreement with the luminosity function inferred from the observations, because

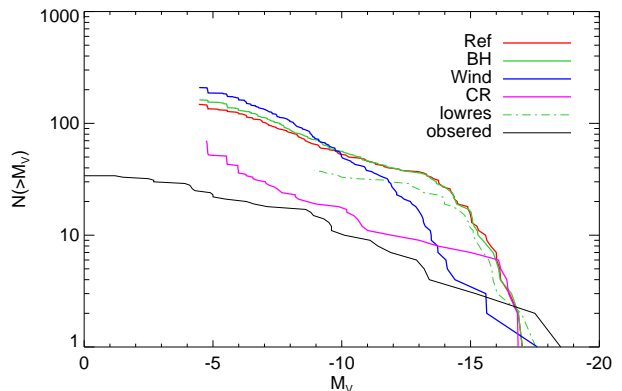


**Figure 2.** Cumulative satellite luminosity function for our different simulation models, compared to the observed luminosity function. Note that the observed luminosity function in this plot includes only known satellites without any incompleteness correction and should thus be seen as a lower limit, especially below  $\approx -7 M_V$  where satellites can only be detected within the 19.4% sky coverage of SDSS.

compared with the reference model the luminosity of the satellites is efficiently suppressed by the CR feedback.

Another view on the satellite abundance is given in Figure 2, where we show the cumulative abundance of the satellite population as a function of luminosity, comparing all four simulation results to the observations. Here, the observational data is based only on direct observations, meaning that the black line should be taken as a lower limit for magnitudes lower than  $\approx -7 M_V$ , because of the incomplete sky coverage of the SDSS. The figure confirms the conclusions we reached from the different results of Fig. 1. The ‘WIND’ simulation is efficient in reducing the luminosity of large satellites of the size of the LMC/SMC, but does not manage to suppress the abundance of low luminosity satellites. In contrast, while the CR simulation does not reduce the luminosity of the brightest satellites much, it is very efficient in suppressing star formation in low-mass subhalos, ultimately producing a much reduced amplitude of the luminosity at the faint end. As a result, the CR simulation stays quite close to the observational data up to the completeness limit of the SDSS.

Figure 2 also includes the result of the ‘LOWRES’ simulation, shown as a green dot-dashed line. We can see that the population of satellite galaxies is independent of resolution to good accuracy up to a magnitude of  $\approx -12 M_V$ . Taking into account that the resolution limit of our high resolution runs is shifted by  $\approx 4$  magnitudes, we expect that our simulated satellite abundance should be numerically converged for satellites brighter than  $\approx -8 M_V$ .

Figure 3 shows yet another way to compare the counts of simulated satellites with the observations. Here we use the maximum circular velocity of satellites,  $v_{\max}$ , on the abscissa, because circular velocities are a good proxy for the (original) mass of the subhalos, but can be much more reliably measured than the mass itself. We note that such velocity functions have already been used in the first discussions of the missing satellite problem, and are still frequently used to compare the number of observed satellites with the sub-

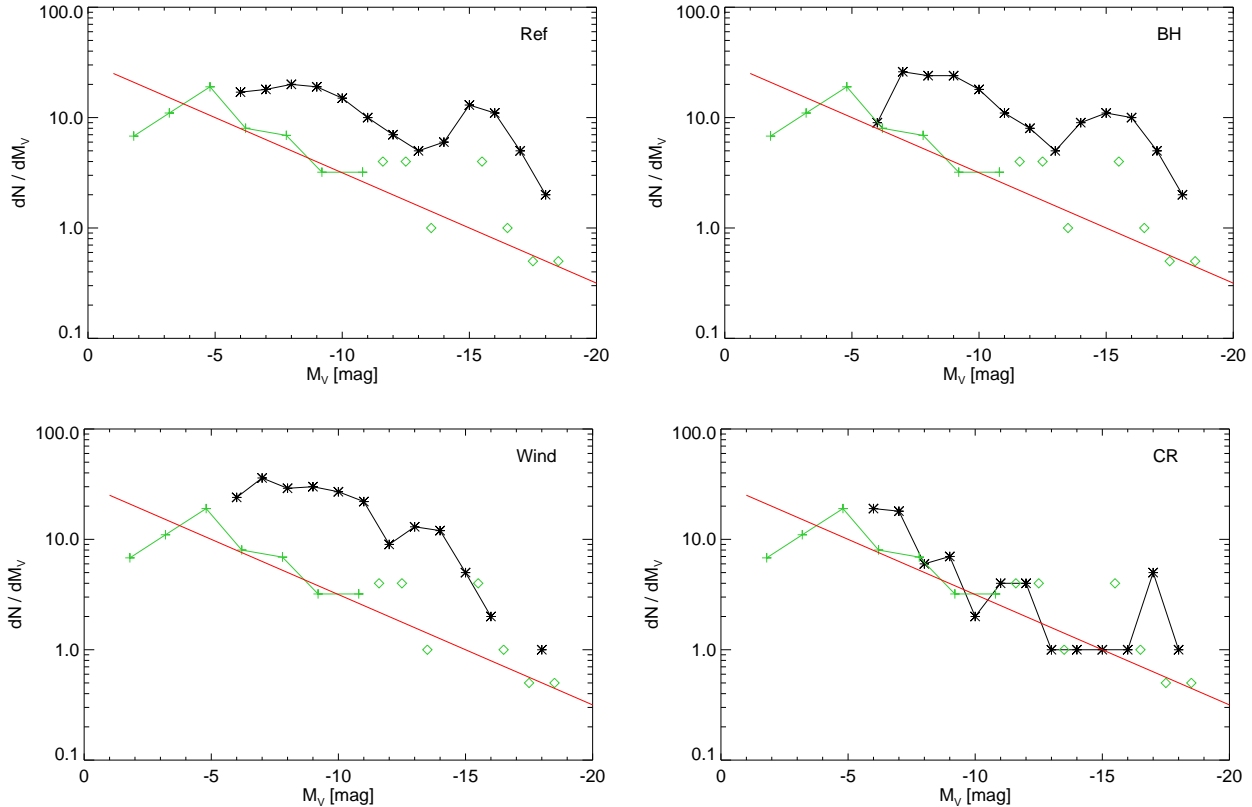


**Figure 1.** The differential luminosity function of the simulated satellites (black curve) compared to the observational data. The latter are represented by the red line, which is the fitting function given by Koposov et al. (2008). The green line shows the scaled luminosity function they obtained for the SDSS satellites while the open diamonds give an extended version using also the luminous satellites of the Milky Way and Andromeda. The different panels show our results for the REF, BH, WIND and CR simulations, respectively.

structure abundance in collisionless N-body simulations (e.g. Madau et al. 2008). The filled green circles in Fig. 3 show the raw observational data, while the open circles are a scaled version that accounts for the SDSS sky coverage and incompleteness. The real cumulative velocity function might thus be expected to lie close to the filled symbols at high circular velocities and to approach the open circles at low circular velocities. The dashed black line shows the cumulative velocity function of all satellite galaxies produced in a dark matter only simulation, using the same initial conditions as for the high resolution hydrodynamical simulations. Finally, the blue line in each panel shows the cumulative mass function of all satellites containing at least  $1 \times 10^4 h^{-1} M_{\odot}$  of stellar mass (one star particle) in the corresponding hydrodynamic simulation.

The differences between the observations and the simulation results for the different physics models appear large at first sight. This however confirms and is consistent with our earlier findings. In particular, the reference simulation and the simulation with black hole feedback overpredict the satellite counts for all velocities, while the wind simulation at least manages to give a reasonable abundance of the brightest satellite systems. Again, we find the cosmic ray simulation to produce the best match to the data. Whereas there may still be a moderate overproduction of bright systems, the extrapolated faint end abundance is matched quite well,

and, in particular, the shape of the predicted luminosity function is in quite good agreement with the observations.

There is another interesting aspect of Figure 3 that concerns the comparison with the dark matter only results. It is a generally assumed that satellite galaxies are dark matter dominated. However, comparing the black dashed line, which shows the mass function of satellites in the corresponding dark matter only simulation starting from the same initial conditions, with the result of the individual hydrodynamic simulations, we note some sizable differences. The high mass satellites show clear evidence that gas cooling has led to a higher concentration of their mass profiles, thereby increasing their circular velocities. Despite the relatively low stellar mass content in these bright satellites, they hence show some structural changes due to baryonic effects. We note however that invoking yet stronger supernovae feedback may reduce these effects if the cooling rate is more effectively reduced.

#### 4.1 Kinematic results

We close this section with an analysis of some of the structural properties of the simulated satellite population. As noted earlier, the total mass of a satellite galaxy is difficult to measure, so other tracers are usually used as a proxy for mass. An observationally readily accessible measure of this type is the central velocity dispersion, which is very commonly



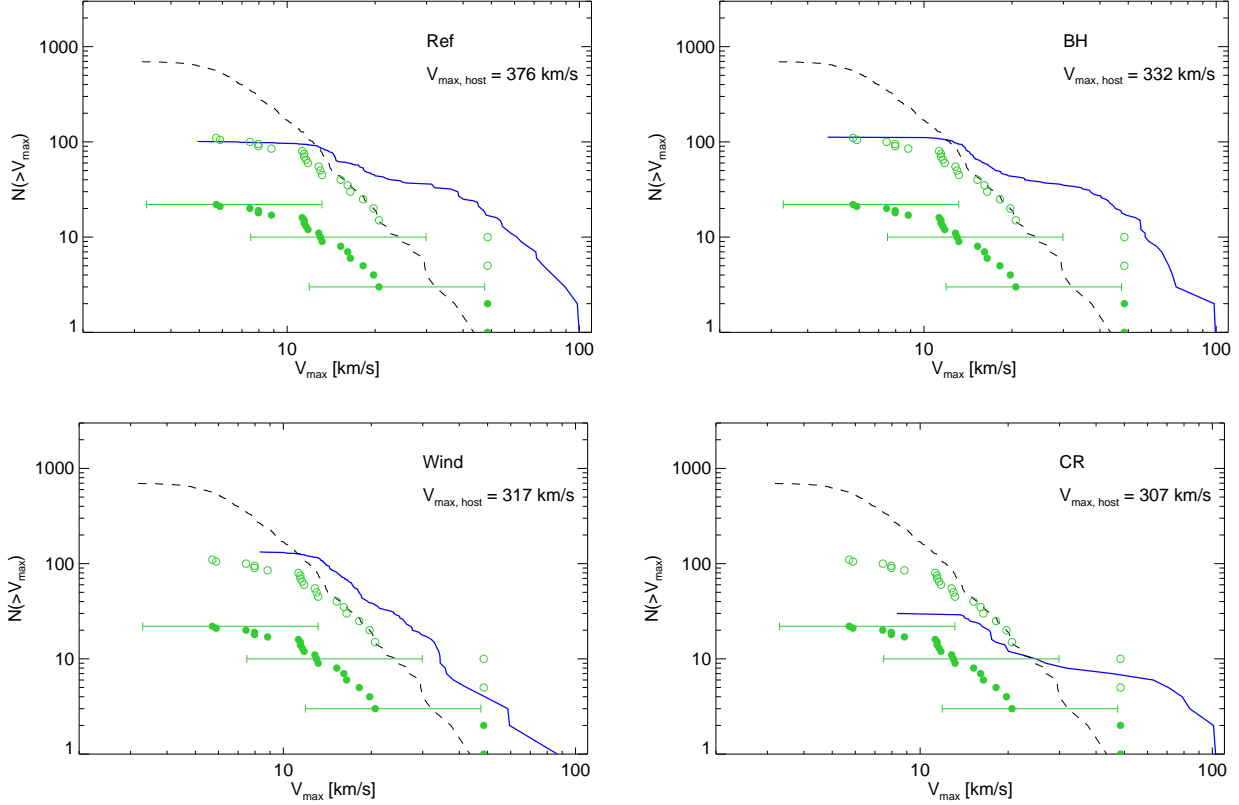


**Figure 3.** The cumulative number of luminous satellites (with stellar mass larger than  $10^5 h^{-1} M_{\odot}$ ) as function of their maximum circular velocity. We compare results for our different physics simulations with data for the Milky Way satellites, taken from Madau et al. (2008); Simon & Geha (2007); Mateo (1998); Martin et al. (2007) and plotted as green filled circles together with the assumption that the circular velocity equals  $\sqrt{3}$  times the central velocity dispersion (Primack 2009). The error bars indicate a plausible range of circular velocities between  $\sigma$  and  $4 \times \sigma$ . Open circles show the same data as the solid circles, but scaled by a factor of 5 to roughly account for SDSS sky coverage and incompleteness. The blue line shows the cumulative mass function of the observable satellites in each hydrodynamical simulation, while for comparison the black dashed line gives the mass function of all substructures in the corresponding dark matter only simulation. The variations in the maximum circular velocity obtained for the host halos in the different simulations are due to the different sizes of the stellar bulges grown in the different runs.

used (e.g. Simon & Geha 2007). In Figure 4, we compare the relation between central velocity dispersion and luminosity for our simulation satellites with data from Simon & Geha (2007), updated with the latest values for the known satellites from Walker et al. (2009).

There seems to be quite good agreement between the observations and the dark matter velocity dispersions of the REF simulation. As the sample of measured satellites is quite small and has rather large error bars, the weak trend of rising velocity dispersion with rising luminosity is not very well determined, but the simulation apparently follows the same trend. We note that the alignment of the simulated satellites on the left hand side of the plot is due to resolution issues from discreteness effects. In fact, the different ‘stripes’ are separated by just one star particle. The stellar mass in each stripe is therefore equal, even though some scatter in luminosity is still present because the luminosity was calculated with the Bruzual & Charlot (2003) model, taking into account the age and metallicity of the star particles, effectively giving each stellar particle its own mass-to-light ratio.

## 5 HISTORY OF SATELLITE GALAXIES

In this section we track the evolution of individual satellites, with the aim to study their formation paths for a range of individual accretion, mass loss and star formation histories. To this end we select nine representative satellite galaxies, split into groups of three that are taken from three different mass ranges. In Figure 5, we show our ‘high mass sample’, consisting of three satellite galaxies with a final stellar mass higher than  $5 \times 10^8 M_{\odot}$ . Satellites with intermediate final stellar mass between  $5 \times 10^8 M_{\odot}$  and  $5 \times 10^6 M_{\odot}$  are shown in Figure 6, while Figure 7 gives three low-mass examples of satellites with a final stellar mass less than  $5 \times 10^6 M_{\odot}$ .

The different panels in the three Figures 5 to 7 are organized in the same way, and show in each case the history of one individual satellite (with a final stellar mass as labeled in the figure). For each satellite, the top panel gives the redshift evolution of the dark matter, gas and stellar components as black, green and red solid lines, respectively. The middle panel shows both the star formation rate (solid line) and the maximum circular velocity (dashed line), as a function of time. Finally, the bottom panel gives the evolution of the radial distance of the satellite to the host galaxy

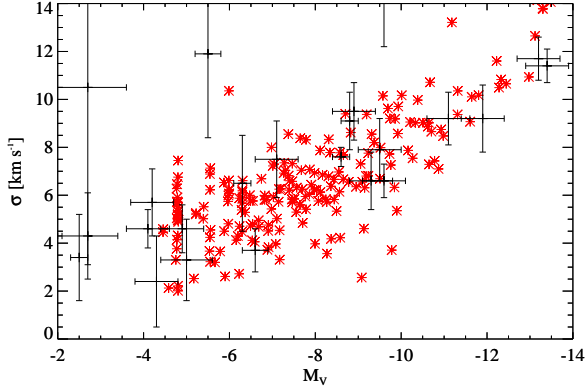


**Figure 4.** Total V-band luminosity against velocity dispersion. We show the observational data points of Simon & Geha (2007) combined with velocity dispersions taken from Walker et al. (2009) as black crosses, and compare to the simulated satellites plotted as red symbols. The two samples are in good agreement, except perhaps for slightly different slopes.

(solid line) and compares this to the virial radius of the host ( $R_{200}$ , dashed line). Finally, the dotted vertical line running through all panels highlights the epoch  $z = 6$ , which is the time when the UV background reionizes the universe in our simulations.

The different satellite histories we have selected in Figs. 5-7 show a variety of interesting evolutionary effects that we now discuss in turn. For definiteness, we have here selected the BH run, but our other simulations show qualitatively very similar results. The left panel of Fig. 5 gives a nice illustration of the tidal and ram pressure stripping effects that play an important role in shaping the properties of the satellites. It is clearly seen that the dark matter mass starts decreasing in distinctive steps as soon as the satellite has fallen into the host halo and orbits with rather high eccentricity. These mass stripping events correspond to individual pericentric passages, as is clearly seen in the panel that gives the distance to the host halo. Note however that the stellar component is not noticeably effected by this tidal stripping process, as expected from the fact that the stars of the satellite are much more concentrated than the dark matter. In contrast, the gas component behaves rather differently. Here we see clear evidence for ram pressure stripping as the dominant source of mass loss even in high mass satellites. Interestingly, this effect starts to set in even before the satellite crosses the virial radius of the host, probably because the gaseous halo of the host is more extended than  $R_{200}$ .

Because ram pressure stripping depends on the density of the surrounding gas, one should expect to see variations of the mass loss rate with the radial position of the infalling satellite. This is indeed seen if one compares the results for the three different satellites shown in Fig. 5 with each other. The satellite on the left follows a very eccentric orbit and spends most of the time in the outer parts of the halo, resulting in a comparatively slow gaseous mass loss. The satellite shown in the middle panel has an orbit with a lower eccentricity that keeps it at apocentre well inside the virial radius, yielding a consistently higher mass loss rate. Finally,

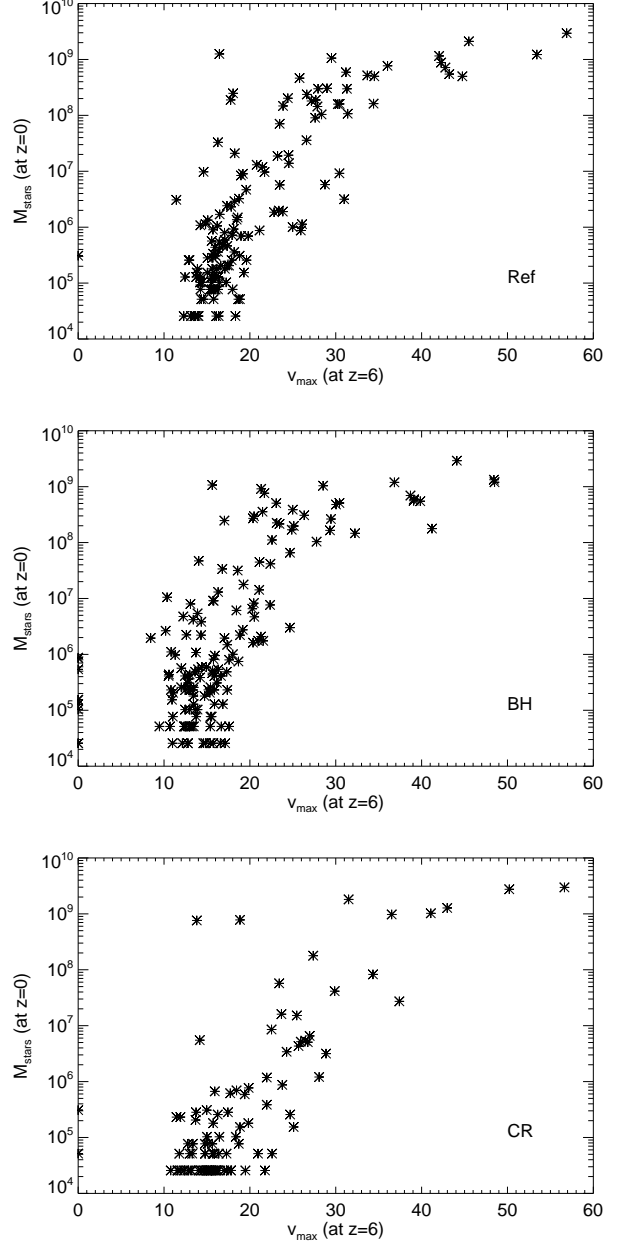


**Figure 8.** Current stellar mass of satellites versus their maximum circular velocity at  $z = 6$ . We do not find a clear threshold in  $v_{\max}$  at  $z = 6$  that could be used to decide whether or not a satellite galaxy is able to form stars later on. Instead, we find that the final stellar mass shows large scatter over a considerable range of circular velocities at the epoch of reionization.

the satellite shown on the right panel has a nearly circular orbit at small radius, and loses its gas component even faster.

Perhaps one of the most interesting effects seen in Figures 5 to 7 is the effect of reionization on the star formation of the satellite galaxies. Quite often the simplifying assumption is made that reionization would be able to stop star formation in satellite galaxies entirely, yet this is clearly in contradiction with the findings of our simulations. In fact, all satellites shown in these Figures (and the same is true for the

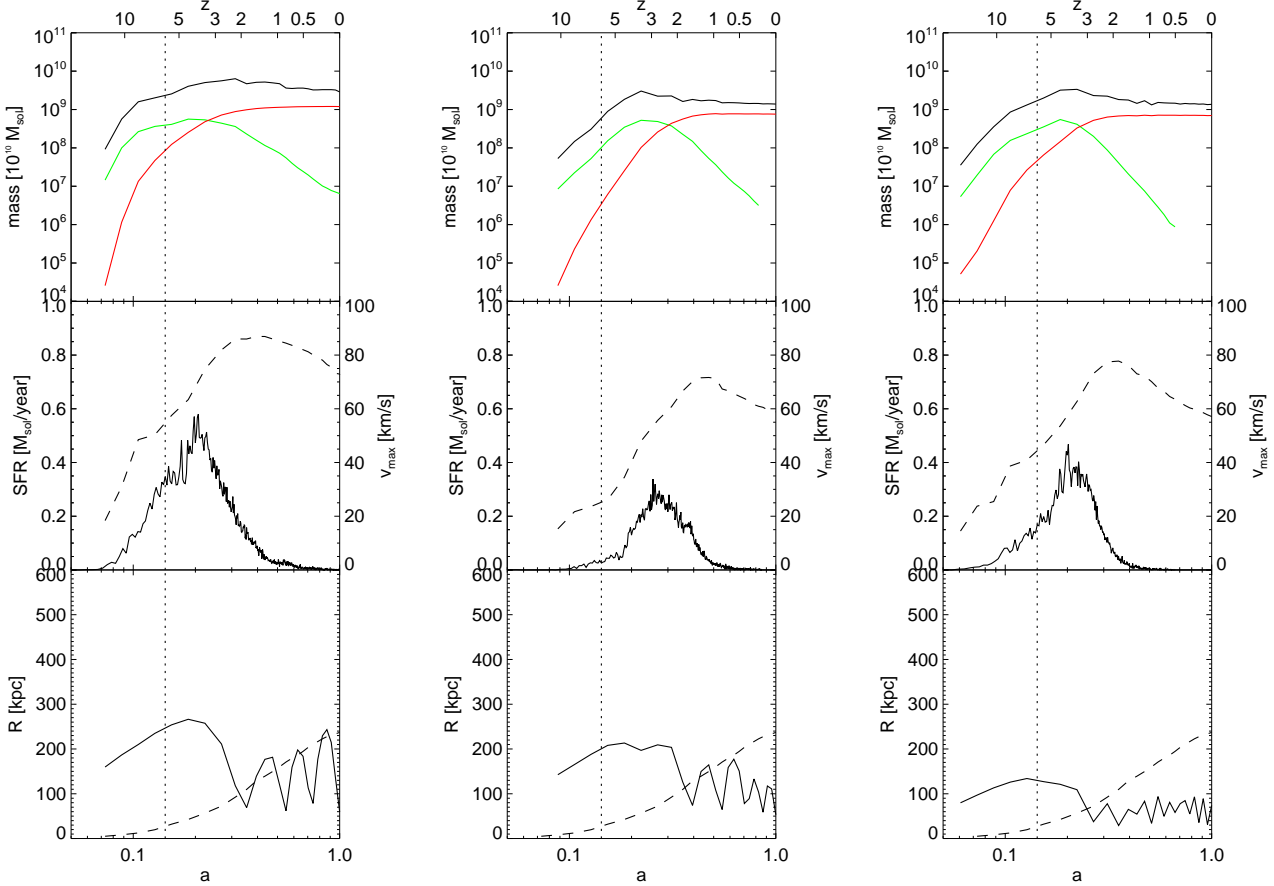


**Figure 5.** Detailed time evolution of three representative examples of high-mass satellites, from the time of their first appearance as individual galaxies until  $z = 0$ . In each case, the top panel shows the evolution of the dark matter, gas and stellar mass components as black, green and red lines, respectively. The middle panel shows the star formation rate as solid line, and the maximum circular velocity as a dashed line (with the corresponding scale on the right  $y$ -axis). The bottom panel gives the radial distance of the satellite to the host galaxy at each timestep (solid line), and compares this to the virial radius ( $R_{200}$ ) shown with a dashed line. The dotted vertical lines in all panels mark the  $z = 6$  epoch of reionization in our simulations.

majority of other satellites too) are producing most of their stars at times later than  $z = 6$ . Star formation continues in all examples until the gas component is removed by ram pressure stripping, but this time can be considerably later than the epoch of reionization. We hence find that the detailed orbit of a satellite galaxies tends to be more important for determining its final luminosity than the circular velocity it had at the epoch of reionization. An illustration of this can be seen in the histories of the satellites shown in the middle and right panels of Figure 6. These two satellites have quite similar dark matter, gas and stellar masses shortly before they enter the hot gaseous halo of the host galaxy, but they are moving on very different orbits. The satellite in the middle panel is on a relatively circular orbit, resulting in a small effect of tidal stripping on the dark matter component and no noticeable effect on the stellar component. In contrast, the satellite shown in the right panel is on a highly eccentric orbit with  $\epsilon \geq 10$ . This satellite dives deeply into the host halo, resulting in a tidal radius that is even smaller than the characteristic radius of the stellar component. Because of this, the stellar component loses nearly 90 % of its mass due to tidal effects.

In Figure 8, we compare the final stellar mass of the satellites against the maximum circular velocity  $v_{\max}$  they had at redshift  $z = 6$ . This provides another way to test the popular hypothesis that the mass at the time of reionization determines the final luminosity of a satellite galaxy. We show results for the simulations REF, BH and CR<sup>†</sup>. While most satellites with circular velocities below  $\sim 20 \text{ km s}^{-1}$  are strongly suppressed in stellar mass, there are a few objects with such low circular velocities that have stellar masses as high as  $10^8 M_{\odot}$ , or even  $10^9 M_{\odot}$ , at the present epoch. In the range of  $\sim 20 \text{ km s}^{-1}$  to  $\sim 30 \text{ km s}^{-1}$ , no sharp cut-off is readily apparent that could be identified with reionization. Instead there is considerable scatter in the relation between final stellar mass and maximum circular velocity at  $z = 6$ . We note that the simulation with cosmic rays shows a strong suppression in the stellar mass for low circular velocities when compared with the other simulations, as expected from our luminosity function results.

<sup>†</sup> Unfortunately, all snapshots before  $z = 2.7$  of the simulation WIND were accidentally deleted, making this comparison impossible for this model.

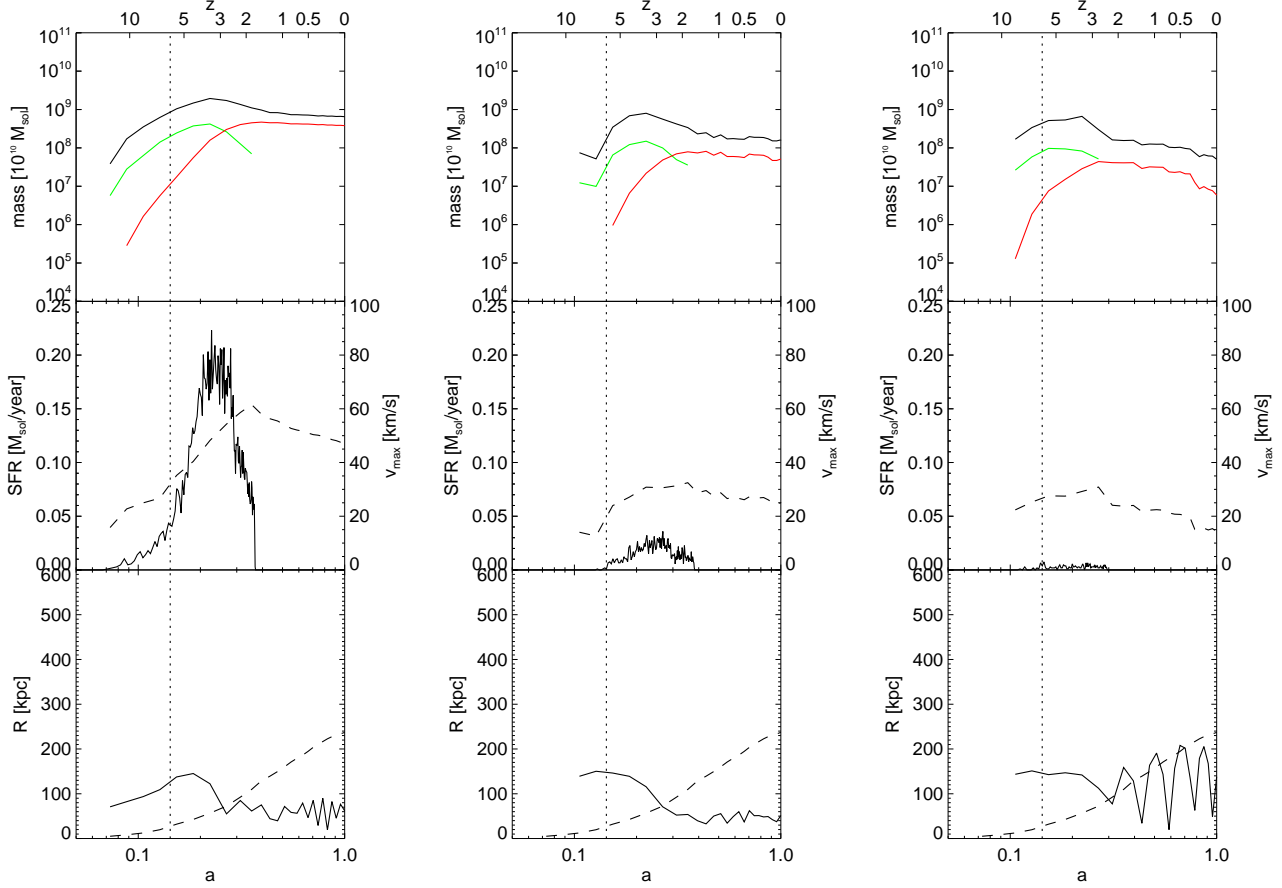


**Figure 6.** The same as Fig. 5, but for three intermediate mass satellites.

A complementary view of the above relation is shown in Figure 9, where we plot the current maximum circular velocity of satellites against their current stellar mass. Different symbols encode the circular velocity they had at redshift  $z = 6$ , where satellites with  $v_{\max} \geq 16 \text{ km s}^{-1}$  at  $z = 6$  are shown as red diamonds while satellites below this threshold are shown as green stars. Note that there is considerable overlap between the regions occupied by the different symbols, showing again that the correlation between the circular velocity at the epoch of reionization and the current stellar mass is not overly strong. In particular, there are some examples (especially in the BH simulation) of satellite galaxies with very low circular velocity at  $z = 6$  which were nevertheless able to form many stars later on and to turn into reasonably luminous satellites.

Finally, in Figure 10, we directly compare the results of the different physics simulations with each other, in terms of the relationship between  $v_{\max}$  and the stellar mass at the time of reionization. Interestingly, we see that AGN feedback is in fact able to reduce the stellar mass formed at high redshift in many of the progenitor systems of today’s satellites, even though the effect is considerably weaker than for cosmic rays. As we have already seen, the influence of BH feedback tends to become however low at later times, so that the present day properties of satellites are only mildly affected. This is presumably because most satellites do simply not grow a massive black hole, but they are nevertheless

affected at high redshift by the seed black hole that is injected into their halo.

In Figure 11, we plot the baryon fraction of satellites against  $v_{\max}$ , at the present epoch. The baryon fraction is here simply defined as the total bound baryonic mass relative to the total bound mass of a halo. It is interesting to compare this value with the universal cosmic baryon fraction  $\Omega_b / (\Omega_b + \Omega_{\text{dm}}) = 0.16$  (shown as dashed horizontal line). As one expects, the baryon fraction is usually lower than the cosmic baryon fraction, especially for very low mass satellites that have lost most of their gas and did not form many stars either. However, in the simulation with comparatively weak feedback, some satellites have also baryon fractions above the cosmic mean value. These are satellites which lost a lot of dark matter through tidal stripping whereas they could hold on to most of their stars. Both the WIND and CR models are leading to considerably reduced baryon fractions in low mass satellites. In the former case, this is readily expected as a signature of the winds. In the latter, it is because more baryons stay in a diffuse gaseous phase, allowing them to be more easily ram-pressure stripped.

An analysis of the evolution of the baryon fraction between  $z = 6$  and  $z = 0$  is given in Figure 12. We here only show results for the REF simulation, as the qualitative behavior of the other simulations is similar. We use two symbols for each satellite, one showing the data point at  $z = 6$  (red stars), while the corresponding values at  $z = 0$

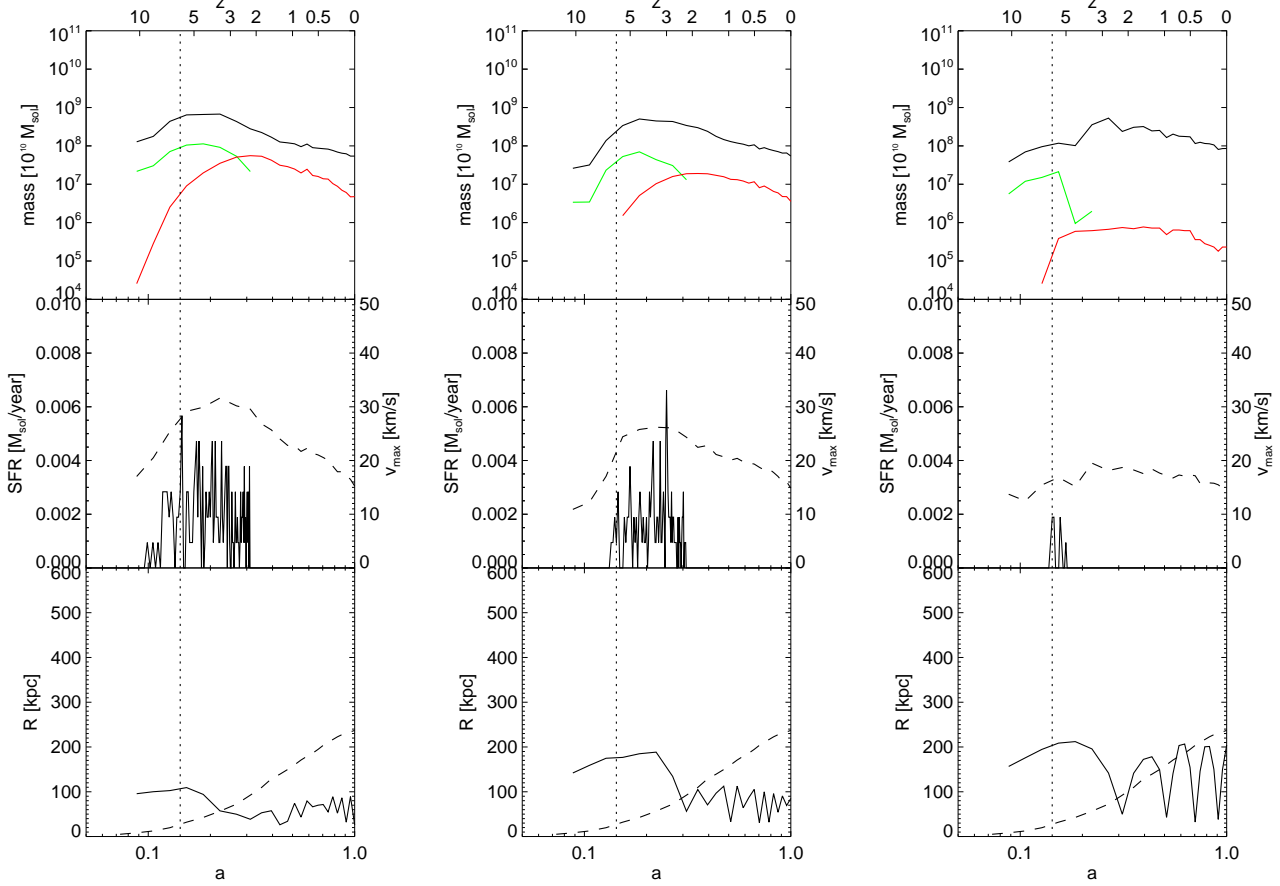


**Figure 7.** The same as Fig. 5 but for three low mass satellites.

are given by green stars. Every pair of points belonging to the same satellite is connected by a dotted line. Most satellites with circular velocities below  $\sim 20 \text{ km s}^{-1}$  at  $z = 6$  lower their baryon fraction substantially until the present epoch, and they also do not tend to grow much. In contrast, most larger satellites tend to keep their baryon fraction or increase it slightly, often accompanied by a significant increase in  $v_{\text{max}}$ . In the most massive satellites, part of this increase stems from modifications of the inner rotation curve due to the formation of a quite concentrated stellar component, i.e. these satellites are not really bona-fide dark matter dominated systems as often assumed. We note however that the threshold at  $\sim 20 \text{ km s}^{-1}$  is not sharp; there are still many examples of satellites with an initially high  $v_{\text{max}}$  that end up as low mass satellites with a stripped baryonic component.

The last quantity we analyze in this section are the cumulative star formation histories of our satellites, as shown in Figure 13. The solid black line shows the total cumulative star formation history of all satellites in the final virial radius, normalized by their total final stellar mass. The gray shaded area gives the  $1\sigma$  scatter around this mean for the ensemble of all satellite star formation histories. The vertical dotted, dashed and dot dashed lines mark the times when 10%, 50% and 90% of the stars present at  $z = 0$  were formed. Finally, the dashed blue line repeats the result of the REF simulation in all the panels corresponding to the

other simulations, in order to ease a comparison between them. As we have already seen in the other results, AGN feedback shows little effect on the cumulative star formation history of the satellites. The WIND model on the other hand leads on an earlier production of the bulk of the stars, which is what one would expect if galactic outflows are efficiently removing gas from star-forming dwarf galaxies and are thus shutting down star formation earlier. In contrast, the CR model shows exactly the opposite effect. Due to the additional pressure component, the galactic gas has a lower overall cooling rate. This hampers star formation in low mass systems but does not by itself remove significant amounts of fuel for star formation; the latter can however be achieved by ram pressure stripping. Thus, star formation shifts to considerably later times in the CR run than in any of the other models.

Interestingly, the scatter around the mean history of the satellites is also modified by the different physics. The WIND simulation shows a rather small scatter, presumably because most satellites form their stars in the first significant phase of star formation at high redshift, which is terminated quickly and for the most part coevally. In the case of the CR simulation, much of the gas is not removed by the primary feedback process itself, but instead is affected by stripping processes at intermediate and low redshifts, after the satellites have fallen into the parent halo. This means that the individual infall history of each satellite is of larger impor-

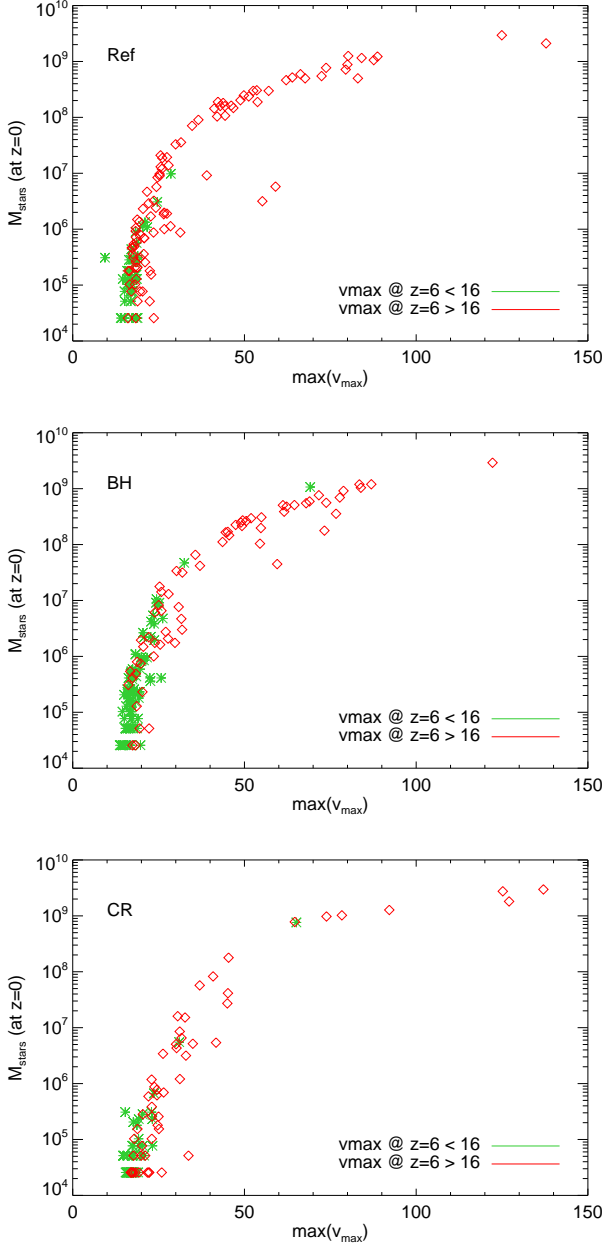


**Figure 9.** Current stellar mass versus current maximum circular velocity. Satellite galaxies with  $v_{\max} \geq 16$  km/s at  $z = 6$  are shown as red diamonds, and satellites below this limit as green stars. There is again no evidence that this threshold or one nearby is able to distinguish between satellites with or without a significant amount of stars.

tance in this model, leading to a higher overall variability in the star formation history of the satellites.

## 6 SCALING RELATIONS

In this section, we investigate in more detail how the properties of our simulated satellites scale with their size. Where possible, we compare with observational results and other theoretical predictions. We want to caution however that especially our smallest luminous satellites are pretty close

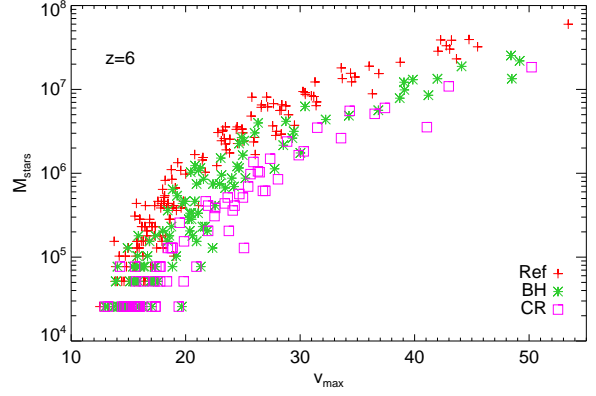


**Figure 10.** Stellar mass versus maximum circular velocity at  $z = 6$ , compared for different simulation models. Interestingly, a weak influence of AGN feedback on the satellite population is found at high redshift, but this difference largely vanishes later on, as most of the satellites are simply not able to grow a large supermassive black hole. In contrast, the additional pressure component of cosmic rays affects all satellites more strongly, and here the effect remains large in small galaxies even down to  $z = 0$ .

to our resolution limit. While the satellites above the detection limits of SDSS should be sufficiently well resolved in our high resolution simulation to give reliable results, a considerable numerical uncertainty persists, a fact that should be taken into account in interpreting the results.

We begin with the scaling relations derived by Woo et al. (2008) for local group dwarf galaxies. We focus on the relations between stellar mass and circular velocity, and stellar mass and star formation rate, as they have the highest statistical significance and are thus best suited to benchmark the simulation results. Figure 14 shows these two relations in separate panels, comparing in each case the fits derived by Woo et al. (2008) with our simulation data. The correlation between stellar mass and maximum circular velocity is comparatively tight, in fact, Woo et al. (2008) cite a correlation coefficient of 0.94 for the observations, which are represented by the solid red line. The simulated satellites show a similarly strong correlation (formally yielding a correlation coefficient of 0.94), but the results for the REF simulation are slightly offset towards higher stellar masses. The CR results (shown with magenta symbols) agree considerably better. Our lowest mass satellites start to deviate from the fit given by Woo et al. (2008) but the differences are of comparable size as in some observed systems such as Ursula Minor, and the growing scatter in the numerical results also indicates that resolution effects start to play a role.

The right panel in Fig. 14 compares the correlations between stellar mass and current star formation rate. Here we find a much worse agreement with the observational results of Woo et al. (2008), which are again characterized by a remarkably good correlation (with coefficient 0.96). While our results bracket the observationally inferred relation, the scatter is large and the formal correlation is only 0.72. In addition, most of our satellite galaxies show only a vanishingly small star formation rate at the present epoch, and those systems were omitted from the plot. But again, the CR results seem to agree better with observations. Simu-

lations with better mass resolution will be needed to shine more light on this potential discrepancy.

Simon & Geha (2007) calculated the mass-to-light ratio for the sample of Milky Way satellites found in the SDSS, obtaining values ranging from about 100 to 1200, with a mean of  $\sim 380$ . Doing the same calculation for the whole sample of known satellites resulted in values between 1.5 and 1200 with a mean of  $\sim 170$ . This suggests that the faint satellites discovered with the SDSS are even more dark matter dominated than the more luminous ‘classical’ satellites. For the complete sample of simulated luminous satellites, we obtain mass-to-light ratios between 12 (11, 16, 10) and 13000 (18000, 23000, 18000) with a mean of  $\sim 1500$  (1350, 1550, 3500) for the REF (BH, WIND, CR) simulation. As mentioned earlier, very small satellites are strongly affected by numerical effects and thus the very large mass-to-light ratios we find for these satellites may be unreliable. Also, the mean value may be biased high by the large number of small satellites. If we restrict the mass-to-light ratio calculation to satellites with  $M_V \leq -8.0$ , we obtain a mean of 232 (217, 315, 345), which is much closer to the observed values. If we select only satellites with a surface brightness  $\mu \leq 30$ , then the mean mass-to-light ratio is 33 (33, 73, 33), which is about 5 times smaller than the observed mean value for this selection.

This difference in the mean mass-to-light ratio can also be seen from the ‘Mateo Plot’ shown in Figure 15, which compares the luminosities of the satellite galaxies with their mass-to-light ratio in units of the solar mass-to-light ratio. In the original paper where this plot was introduced, Mateo (1998) overplotted the function

$$\log \frac{(M/L)}{(M/L)_\odot} = 2.5 + 10^7 / (L/L_\odot), \quad (5)$$

which we also included as the dark red dot-dashed line in Fig. 15. To guide the eye, we also simply scaled this function by a factor of  $\approx 5.2$  and plotted it again as the purple dot-dashed line. It can be seen that this scaled function fits the simulated galaxies of the REF simulation very well, while the observed systems (shown with red and green triangles) are well described by the original function. This result is consistently reproduced by all simulations. Only the constant horizontal offset between observations and simulations changes by  $\approx 10\%$  while the general trend remains the same.

We note that the nearly constant offset between the simulated and observed satellite galaxies could in part be caused by the rather uncertain procedure applied to estimate the total mass of observed satellites. This effectively involves an extrapolation to the outer edge of the satellite, which is uncertain. An alternative would be that the simulated galaxies simply contain fewer stars than expected for an observed satellite of the same mass. However, the REF simulation already has comparatively weak feedback, and allowing for brighter satellites by a constant factor would cause the most luminous satellites, which are in good agreement with the Magellanic Clouds, to become too bright. Furthermore, making the star formation more efficient in all satellites would shift the points in Fig. 15 both down and to the right, hence spoiling the good agreement with the location of the break in the observed relation.

In Figure 16, we show the relation between photometric surface brightness of all simulated dwarf galaxies inside

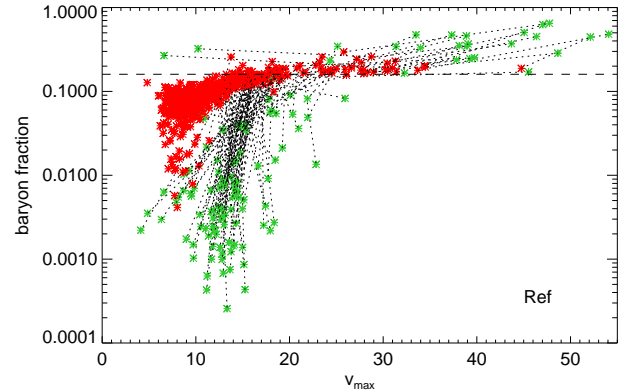


**Figure 12.** Evolution of the baryon fraction and circular velocity between  $z = 6$  and  $z = 0$ . For each satellite, we mark the high redshift  $z = 6$  data with a red star and the  $z = 0$  value with a green star, and we connect each pair of two points with a dotted line. There is clearly a pivotal maximum circular velocity of about  $\sim 25 \text{ km s}^{-1}$  below which most satellites lose a large fraction of their baryons, while they retain their baryon fraction above this threshold.

a sphere of radius 350 kpc centred on a fiducial position of the Sun. The Sun was assumed to lie 8.5 kpc away from the centre of the galaxy, in the central plane of the stellar disc. As can be seen from the relatively large scatter of the plot, the simulation produces also satellites that are well above the SDSS surface brightness detection limit. Counting the galaxies with a photometric magnitude brighter than  $30 \text{ mag/arcsec}^2$  (dashed red line) and a distance smaller than 280 kpc (dot dashed blue line) results in observable 46 (77, 18, 70) satellites for the REF (BH, CR, WIND) simulation. This is actually in reasonable agreement with the prediction of 57 satellites for the Milky Way. The cutoff radius of 280 kpc was chosen as a compromise between the measured distances to all known satellites, which reach up to  $\approx 1 \text{ Mpc}$ , and the virial radius of  $r_{200} = 238 \text{ kpc}$  of the simulated host galaxy. This is also the same cut off radius that has been used in previous work (Koposov et al. 2008; Macciò et al. 2010), although we note that some studies have adopted a different choice (e.g. Diemand et al. 2007). The rather small number of satellites classified as ‘observable’ for the CR simulation can easily be explained by the lower luminosity function shown in figure 1.

Finally, we consider the relation between the dark matter masses of our simulated satellites with their stellar mass and luminosity, as shown in Figure 17. For each satellite, we plot the dark matter mass with different symbols, both at the epoch of accretion and at the present epoch. To simplify a comparison with figure 5 of Macciò et al. (2010), we used exactly the same axis range in our plot as they did. Unlike in the results of Macciò et al. (2010), we find a clear bend in the relation, meaning that our satellites tend to have higher stellar masses, especially at the low mass end, than the satellites of Macciò et al. (2010). The latter results are based on a semi-analytic model where the orbits of an infalling satellite are estimated based on a random choice of plausible infall parameters. It is possible that this explains the discrepancy, or that it originates in approximate treatments of tidal or ram pressure stripping in the semi-analytic model. In future

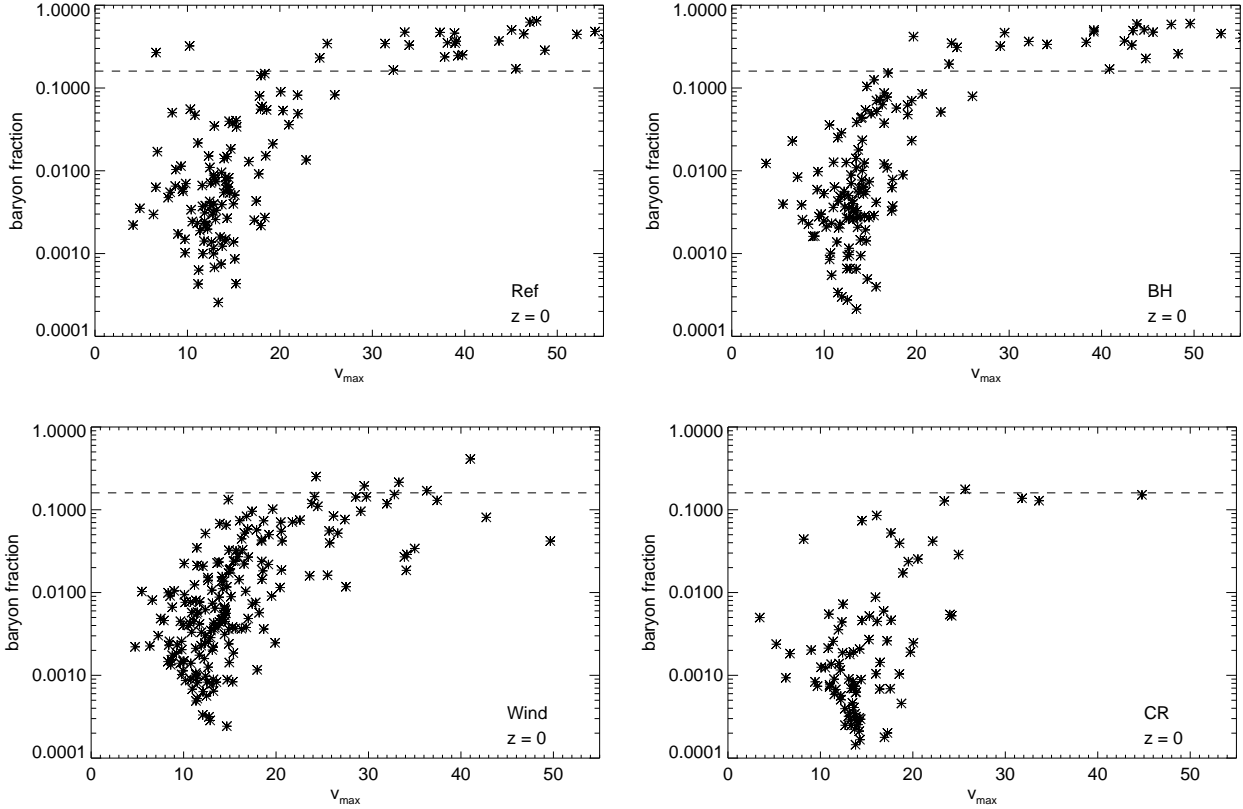


**Figure 11.** Baryon fraction of  $z = 0$  satellite galaxies as a function of their circular velocity. We show results for our four primary simulation models, and define the baryon fraction in terms of the bound particles identified by SUBFIND for each satellite. The horizontal dashed line gives the universal cosmic baryon fraction.

work, it will be interesting to inter-compare direct hydrodynamical simulations and the semi-analytic models on a satellite by satellite basis, in order to better understand the origin of these differences in the predictions.

## 7 CONCLUSIONS

In this work, we studied a set of high-resolution hydrodynamical simulations of the formation of a Milky Way sized galaxy, starting from cosmological initial conditions. Such simulations are now able to reach sufficiently high resolution to directly resolve the formation of the small dwarf galaxies that orbit in the halo, thereby allowing studies of the missing satellite problem and of the properties predicted by simulations for the population of satellite galaxies. These galaxies are especially interesting both because the dark matter substructure abundance is a fundamental challenge for the  $\Lambda$ CDM cosmology, and because the low star formation efficiencies of the satellites provide crucial information about the physics of feedback.

We have therefore repeated our simulations using different models for feedback physics, with the goal to test the sensitivity of the results for the satellites with respect to these physics assumptions. In the REF model, we considered only star formation and SN feedback, together with instantaneous reionization at  $z = 6$ . The three other models included additional processes like AGN feedback (BH),

wind driven galactic outflows (WIND) and the generation and decay of cosmic rays (CR). Not unexpectedly, the BH model showed no significant differences compared to the reference REF model, as most of the satellites are simply too small to grow a large supermassive black hole and are rarely affected by strong quasar feedback in neighbouring galaxies. In contrast, the WIND model showed a significant reduction of the number of high mass satellites, but did not give a significantly different abundance of low mass systems. The CR model had exactly the opposite effect as it did not change the high mass satellites but suppressed star formation in low mass satellites. This made the cosmic ray model most successful in matching the faint-end of the observed satellite luminosity function. Our results further suggest that a combination of the WIND and CR feedback models should be able to yield a nearly perfect match of the luminosity function.

The total number of satellites observable with an SDSS-like survey covering the whole sky has been estimated to be 57 (Simon & Geha 2007). Interestingly, imposing the same surface brightness detection threshold on all of our simulated systems yields a prediction of 77 observable satellites for our BH model, which is only moderately higher than the observations despite the fact that this simulation overpredicts the satellite luminosity function considerably. For our CR model instead, the number drops considerably, to 18, perhaps caused in part by an overprediction of the effective stellar radii of the satellites, which could easily arise



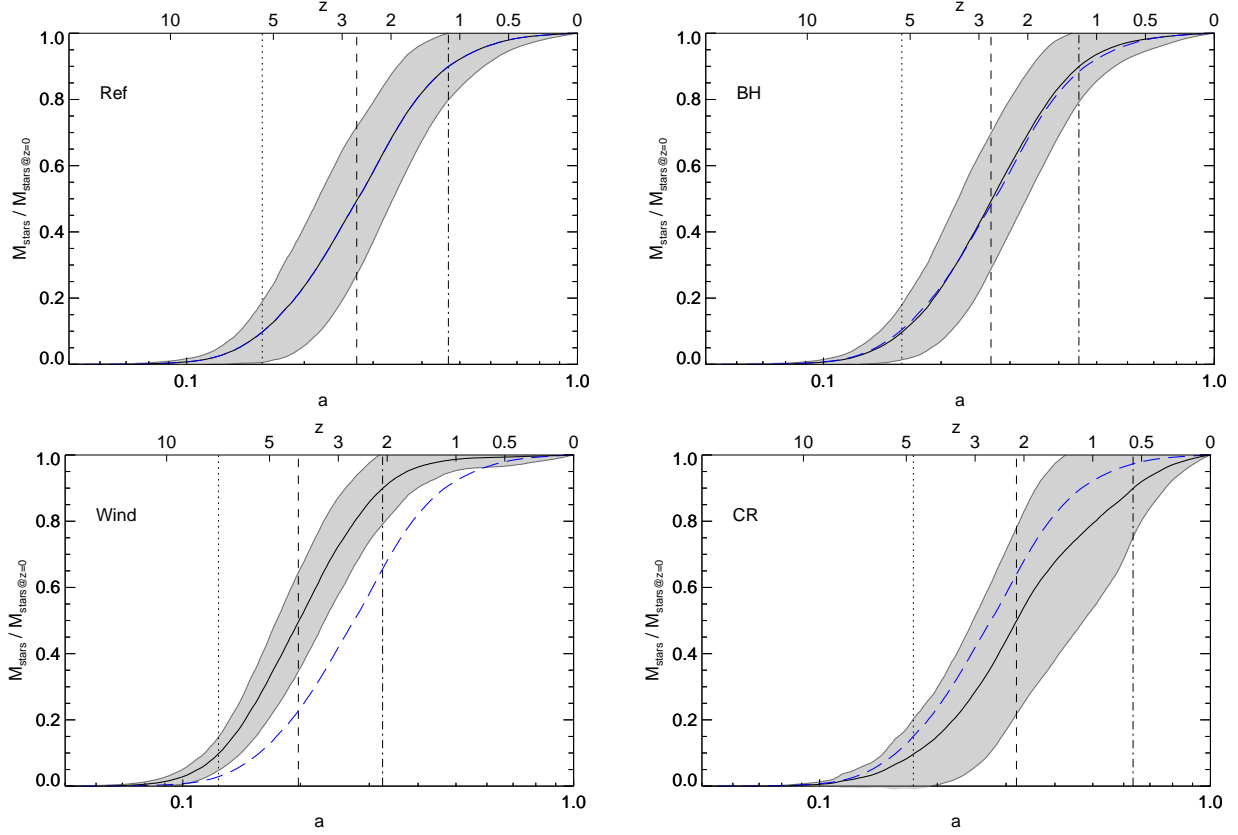


**Figure 13.** Average cumulative star formation histories of all satellite galaxies, for all four primary simulation models. In each panel, the solid line shows the average star formation history, with the grey bands mark the  $1\sigma$  scatter of the distribution. The vertical dashed and dotted lines give the times when 10%, 50%, and 90% of all the stars have formed. To ease the comparison between the different simulations, the result of the REF simulation is repeated in all the panels as a dashed blue line.

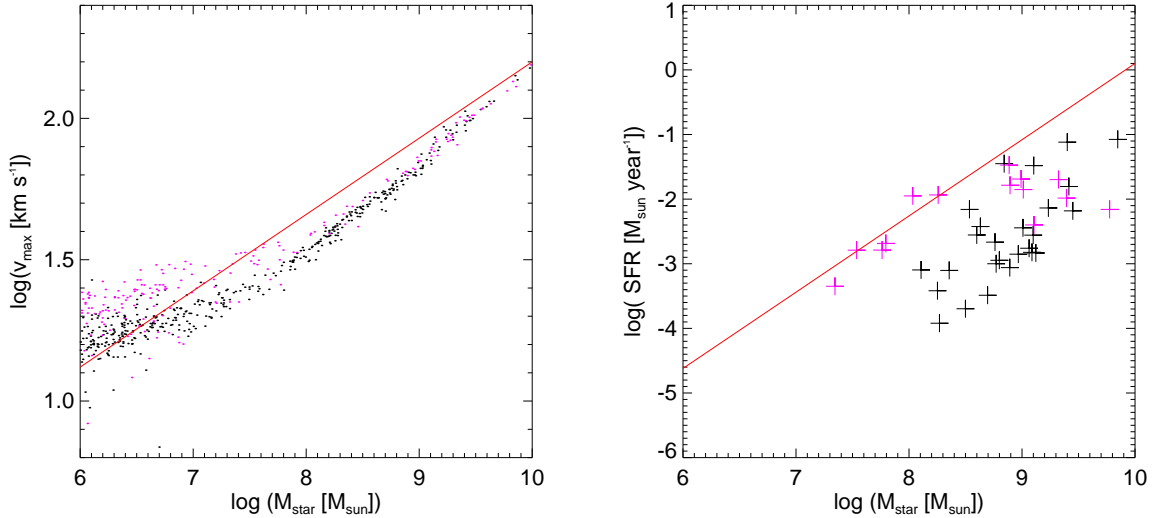


**Figure 14.** The left panel shows the relation between stellar mass and maximum circular velocity at the present time, while the right panel gives the relation between stellar mass and star formation rate. The red lines give the best fits Woo et al. (2008) derived for the observational data. We here included all simulated dwarf galaxies within the full high resolution region of the REF simulation (in black) and of the CR simulation (in magenta), since Woo et al. (2008) did also include dwarfs outside of the virial radius of the Milky Way.

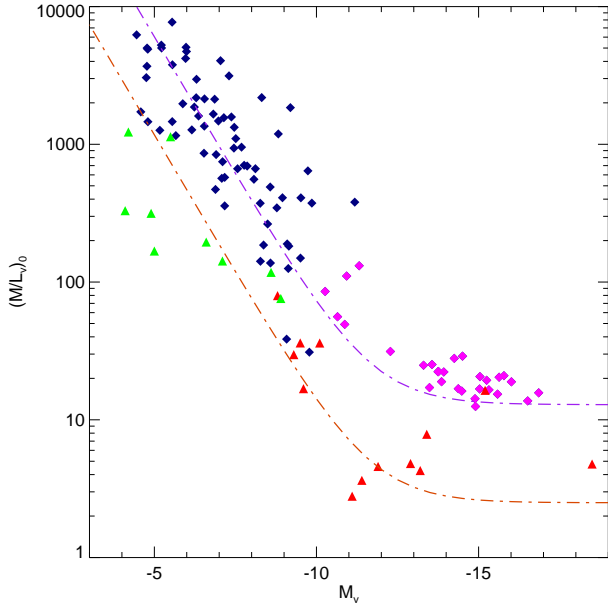


**Figure 15.** The relation between mass-to-light ratio and luminosity of satellite galaxies (see Mateo 1998). The observed satellites are plotted as triangles, with red symbols marking satellites known before SDSS and green symbols marking the newly discovered satellites discovered in the SDSS data. Diamonds give our simulated satellites (REF model), colour-coded as magenta if their surface brightness is high ( $\mu \geq 30$ ) or as dark blue if it is low. The dot-dashed lines represent the fitting function suggested by Mateo (1998), for the observed sample (red) and shifted upwards by a factor of 5 (dark purple) to match the simulated sample.

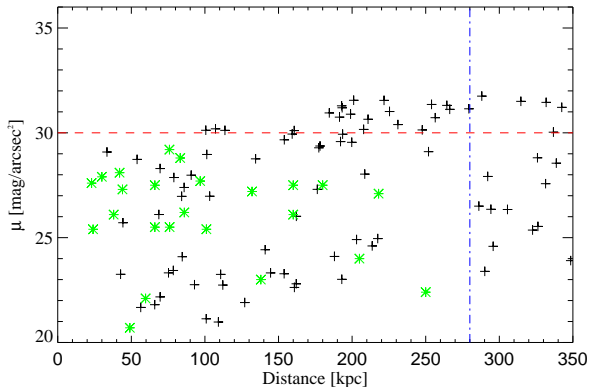


**Figure 16.** Photometric V-band surface brightness of the simulated satellites (black crosses), inside a sphere of radius 350 kpc around a fiducial position of the Sun in the simulations. The red line shows the surface brightness detection limit of the SDSS survey, while the blue vertical line gives the radial cut at 280 kpc that we frequently used in this work. There are 46 Satellites below this limit within a radius of 280 kpc which is relatively close to the 57 satellites predicted for an all-sky extrapolation of the observational data. The green stars give the observed satellites with well determined surface brightnesses.

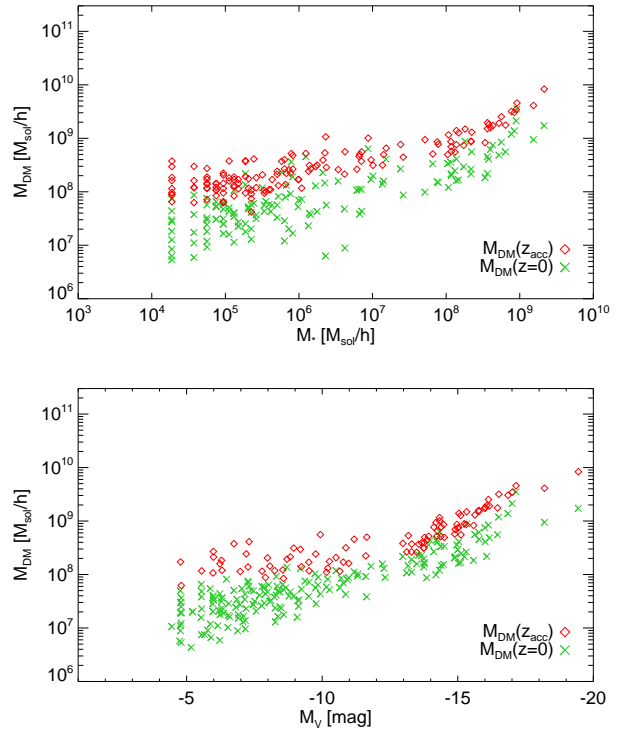


**Figure 17.** Relation between dark matter satellite mass and stellar mass, or stellar luminosity, respectively. For each satellite we show both the dark matter mass today and at redshift  $z = 6$ . This plot may be compared directly to figure 5 of Macciò et al. (2010), which is representative for semi-analytic models constructed to describe the satellite population. Unlike in their results, there is clearly some curvature found with the hydrodynamical simulation in this relation.

from the limited spatial resolution of our simulations. In any case, this stresses that a large number of additional satellites may actually still be hidden just below the surface brightness limit of the SDSS (see also Bullock et al. 2009).

Our simulations have also highlighted the relative importance of some of the evolutionary aspects of satellite galaxies. In particular, we do not find a very distinctive mark of the epoch of reionization on the satellites, and most satellites continue their star formation activity in our simulations to much lower redshift than  $z = 6$ . This suggests that simplified treatments of satellite histories, where relatively high cooling thresholds due to a ionizing UV background are invoked, are not particularly realistic. Our simulation results agree much better with the scenario outlined in Strigari et al. (2007), which in fact resembles many of our simulation findings quite closely.

We find that the observed relationship between V-band luminosity and velocity dispersion is quite well reproduced by our simulations, albeit with large scatter. The small amount of reliable observational data for the velocity dispersions leaves it unclear at present whether the larger scatter we find indicates a problem of the simulations or whether is also present in reality. What is comparatively clear though is that the observed relation between stellar mass and maximum circular velocity is really tight, a finding that is also reproduced by our simulation results. On the other hand, the

correlation between present-day stellar mass and star formation rate seen in our simulations seems to be not nearly as well-defined as in the observational data. This is related to the fact that we do not find a good correlation between the present stellar and gaseous masses; many simulated satellites have comparable stellar masses but differ in their gas fractions by huge factors. Gas-rich and completely gas-depleted satellites coexist in the same total and stellar mass regime, rendering a tight correlation with the star formation rate unlikely.

But perhaps the most significant discrepancy between the simulation results and observations lies in the inferred mass-to-light ratios. The mass-to-light ratios of the simulated galaxies are off by about a factor of 5 when compared at face value to the observational estimates. This means that they are either too massive, or too faint for their mass. The discrepancy could also be caused by a systematic underestimate of the total satellite masses in the observations. Due to the difficulty of reliably determining the ‘outer edge’ of the dark matter halo of an orbiting satellite, this possibility cannot be easily excluded.

In summary, we find that the current generation of cosmological hydrodynamic simulations is able to explain many properties of the observed satellite population surprisingly well. We have shown that different feedback physics affects the satellite population strongly, with respect to quantities such as luminosity function, scaling relations, or star formation histories. This emphasizes the significant potential of “near-field cosmology” within our Local Group to inform the general theory of galaxy formation. Our work has also shown that it is not necessarily the physics of cosmic reionization and supernova feedback alone that is responsible for resolving the missing satellite problem. In fact, the role of reionization has probably been grossly overstated in many previous works, while other important feedback, such as cosmic rays, has been ignored. It will therefore be very interesting to refine the hydrodynamical simulations further in future work, and to make them more faithful in capturing all the relevant physics.

## 8 ACKNOWLEDGEMENTS

This research was supported by the DFG cluster of excellence ‘Origin and Structure of the Universe’.

## REFERENCES

- Aharonian F., Akhperjanian A. G., Bazer-Bachi A. R., et al., 2006, *Nature*, 439, 695
- Bekki K., 2008, *ApJ*, 684, L87
- Belokurov V., Walker M. G., Evans N. W., et al., 2008, *ApJ*, 686, L83
- Belokurov V., Walker M. G., Evans N. W., et al., 2009, *MNRAS*, 397, 1748
- Belokurov V., Walker M. G., Evans N. W., et al., 2010, *ArXiv e-prints*
- Belokurov V., Zucker D. B., Evans N. W., et al., 2006, *ApJ*, 647, L111
- Belokurov V., Zucker D. B., Evans N. W., et al., 2007, *ApJ*, 654, 897
- Benson A. J., Frenk C. S., Lacey C. G., Baugh C. M., Cole S., 2002, *MNRAS*, 333, 177
- Bruzual G., Charlot S., 2003, *MNRAS*, 344, 1000
- Bullock J. S., Stewart K. R., Kaplinghat M., Tollerud E. J., 2009, *ArXiv e-prints*
- Busha M. T., Alvarez M. A., Wechsler R. H., Abel T., Strigari L. E., 2010, *ApJ*, 710, 408
- Colín P., Avila-Reese V., Valenzuela O., 2000, *ApJ*, 542, 622
- Croton D. J., Springel V., White S. D. M., et al., 2006, *MNRAS*, 365, 11
- Dekel A., Silk J., 1986, *ApJ*, 303, 39
- Di Matteo T., Springel V., Hernquist L., 2005, *Nature*, 433, 604
- Diemand J., Kuhlen M., Madau P., 2007, *ApJ*, 657, 262
- Diemand J., Kuhlen M., Madau P., et al., 2008, *Nature*, 454, 735
- Dolag K., Borgani S., Murante G., Springel V., 2009, *MNRAS*, 399, 497
- Enßlin T. A., Pfrommer C., Springel V., Jubelgas M., 2007, *A&A*, 473, 41
- Gilmore G., Wilkinson M. I., Wyse R. F. G., et al., 2007, *ApJ*, 663, 948
- Gnedin N. Y., 2000, *ApJ*, 542, 535
- Grebel E. K., 2000, in *Star Formation from the Small to the Large Scale*, edited by F. Favata, A. Kaas, A. Wilson, vol. 445 of *ESA Special Publication*, 87
- Haardt F., Madau P., 1996, *ApJ*, 461, 20
- Hoefl M., Yepes G., Gottlöber S., Springel V., 2006, *MNRAS*, 371, 401
- Hopkins P. F., Hernquist L., Cox T. J., Di Matteo T., Robertson B., Springel V., 2006, *ApJS*, 163, 1
- Irwin M. J., Belokurov V., Evans N. W., et al., 2007, *ApJ*, 656, L13
- Jubelgas M., Springel V., Ensslin T., Pfrommer C., 2008, *A&A*, 481, 33
- Katz N., Weinberg D. H., Hernquist L., 1996, *ApJS*, 105, 19
- Kennicutt Jr. R. C., 1989, *ApJ*, 344, 685
- Klypin A., Kravtsov A. V., Valenzuela O., Prada F., 1999, *ApJ*, 522, 82
- Koposov S., Belokurov V., Evans N. W., et al., 2008, *ApJ*, 686, 279
- Kravtsov A. V., Gnedin O. Y., Klypin A. A., 2004, *ApJ*, 609, 482
- Li Y., De Lucia G., Helmi A., 2010, *MNRAS*, 401, 2036
- Liu C., Hu J., Newberg H., Zhao Y., 2008, *A&A*, 477, 139
- Longair M. S., 1999, *Galaxy Formation*, Springer, Berlin
- Macciò A. V., Fontanot F., 2010, *MNRAS*, L28
- Macciò A. V., Kang X., Fontanot F., Somerville R. S., Koposov S., Monaco P., 2010, *MNRAS*, 402, 1995
- Madau P., Diemand J., Kuhlen M., 2008, *ApJ*, 679, 1260
- Martin N. F., de Jong J. T. A., Rix H.-W., 2008, *ApJ*, 684, 1075
- Martin N. F., Ibata R. A., Chapman S. C., Irwin M., Lewis G. F., 2007, *MNRAS*, 380, 281
- Mateo M. L., 1998, *ARA&A*, 36, 435
- Moore B., Ghigna S., Governato F., et al., 1999, *APJ*, 524, L19
- Okamoto T., Frenk C. S., 2009, *MNRAS*, 399, L174
- Okamoto T., Gao L., Theuns T., 2008, *MNRAS*, 390, 920
- Oppenheimer B. D., Davé R., 2006, *MNRAS*, 373, 1265

- Pfrommer C., 2008, MNRAS, 385, 1242
- Pfrommer C., Enßlin T. A., Springel V., 2008, MNRAS, 385, 1211
- Pfrommer C., Enßlin T. A., Springel V., Jubelgas M., Dolag K., 2007, MNRAS, 378, 385
- Primack J. R., 2009, New Journal of Physics, 11, 10, 105029
- Scannapieco C., White S. D. M., Springel V., Tissera P. B., 2009, MNRAS, 396, 696
- Scannapieco E., Thacker R. J., Davis M., 2001, ApJ, 557, 605
- Simon J. D., Geha M., 2007, ApJ, 670, 313
- Springel V., 2005, MNRAS, 364, 1105
- Springel V., Di Matteo T., Hernquist L., 2005, MNRAS, 361, 776
- Springel V., Hernquist L., 2002, MNRAS, 333, 649
- Springel V., Hernquist L., 2003, MNRAS, 339, 289
- Springel V., Wang J., Vogelsberger M., et al., 2008, MNRAS, 391, 1685
- Springel V., White S. D. M., Tormen G., Kauffmann G., 2001, MNRAS, 328, 726
- Stadel J., Potter D., Moore B., et al., 2009, MNRAS, 398, L21
- Stoehr F., White S. D. M., Tormen G., Springel V., 2002, MNRAS, 335, L84
- Strigari L. E., Bullock J. S., Kaplinghat M., et al., 2008, Nature, 454, 1096
- Strigari L. E., Bullock J. S., Kaplinghat M., Diemand J., Kuhlen M., Madau P., 2007, ApJ, 669, 676
- Strigari L. E., Frenk C. S., White S. D. M., 2010, ArXiv e-prints
- Thacker R. J., Scannapieco E., Davis M., 2002, ApJ, 581, 836
- Tollerud E. J., Bullock J. S., Strigari L. E., Willman B., 2008, APJ, 688, 277
- van den Bergh S., 1994, AJ, 107, 1328
- van den Bergh S., 2000, The galaxies of the local group, Cambridge Univ. Press, Cambridge
- Walker M. G., Mateo M., Olszewski E. W., Peñarrubia J., Wyn Evans N., Gilmore G., 2009, ApJ, 704, 1274
- Walsh S. M., Jerjen H., Willman B., 2007, ApJ, 662, L83
- Walsh S. M., Willman B., Sand D., et al., 2008, APJ, 688, 245
- Watkins L. L., Evans N. W., Belokurov V., et al., 2009, MNRAS, 398, 1757
- White S. D. M., Rees M. J., 1978, MNRAS, 183, 341
- Willman B., Blanton M. R., West A. A., et al., 2005a, AJ, 129, 2692
- Willman B., Dalcanton J., Ivezić Ž., et al., 2002, AJ, 123, 848
- Willman B., Dalcanton J. J., Martinez-Delgado D., et al., 2005b, ApJ, 626, L85
- Woo J., Courteau S., Dekel A., 2008, MNRAS, 390, 1453
- York D. G., Adelman J., Anderson Jr. J. E., et al., 2000, AJ, 120, 1579
- Zucker D. B., Belokurov V., Evans N. W., et al., 2006a, ApJ, 650, L41
- Zucker D. B., Belokurov V., Evans N. W., et al., 2006b, ApJ, 643, L103